
ExGRG: Explicitly-Generated Relation Graph for Self-Supervised Representation Learning

Mahdi Naseri

*Department of Electrical and Computer Engineering
University of Waterloo*

mahdi.naseri@uwaterloo.ca

Mahdi Biparva

Huawei Noah's Ark Lab

mahdi.biparva@huawei.com

Abstract

Self-supervised Learning (SSL) has emerged as a powerful technique in pre-training deep learning models without relying on expensive annotated labels, instead leveraging embedded signals in unlabeled data. While SSL has shown remarkable success in computer vision tasks through intuitive data augmentation, its application to graph-structured data poses challenges due to the semantic-altering and counter-intuitive nature of graph augmentations. Addressing this limitation, this paper introduces a novel non-contrastive SSL approach to **Explicitly Generate** a compositional **Relation Graph** (ExGRG) instead of relying solely on the conventional augmentation-based implicit relation graph. ExGRG offers a framework for incorporating prior domain knowledge and online extracted information into the SSL invariance objective, drawing inspiration from the Laplacian Eigenmap and Expectation-Maximization (EM). Employing an EM perspective on SSL, our E-step involves relation graph generation to identify candidates to guide the SSL invariance objective, and M-step updates the model parameters by integrating the derived relational information. Extensive experimentation on diverse node classification datasets demonstrates the superiority of our method over state-of-the-art techniques, affirming ExGRG as an effective adoption of SSL for graph representation learning.

1 Introduction

In supervised deep learning, models are traditionally trained using annotated data. Recognizing the high cost involved, SSL methods capitalize on the abundance of readily available unlabeled data. The underlying principle is to leverage existing signals within the data distribution for pre-training parametric deep models. SSL techniques typically involve applying data augmentations to input samples. An invariance objective is formulated to encourage identical representations for a pair of random views originating from the same source sample.

In computer vision, data augmentations are straightforward and intuitive. They include operations like cropping, rotation, noise adding, and color jittering. On the contrary, the data augmentation in the graph domain is not as intuitive as in vision. Particularly in node classification, common augmentations include node feature masking and edge dropout, which heavily rely on the specific characteristics of the data distribution. Forming representations based on masking certain features may seem counter-intuitive to domain experts, leading to semantic-altering augmentations (Lee et al., 2022). Adding or removing random edges to the source graph can significantly impact the structural properties of the graph (Sun et al., 2021; Lee et al., 2022). Thus, relying on invariance loss solely based on graph augmentation is misleading and lacks the necessary information to learn robust representations.

To alleviate the shortcomings of data augmentation, our work proposes integrating additional appropriate information derived from the input graph. This aids in determining which data samples are candidates to share similar representations. Rather than the prevailing rigid binary determination of whether two points should share a similar representation or not, we embrace a soft, probabilistic evaluation of the degree of similarity. Given the inadequacy and misguidance of graph augmentations, alternative cues are incorporated to guide the determination of analogous representations and assess the relative significance of each pairwise comparison. To achieve this, we propose explicitly generating

a higher-order compositional relation graph that pinpoints crucial relation pairs, serving as candidates for the invariance loss. We propose a comprehensive strategy for constructing this compositional relation graph, leveraging insights from three key sources, each contributing to its distinct relation graph: (i) *Neighborhood Similarity in the Representation Space*, (ii) *Higher-Order Graph Encodings*, encompassing the source graph adjacency alongside diverse positional and structural encodings (PSEs), and (iii) *A Deep Clustering* module. We enrich the learning process, elevating the acquired representation and mitigating the deficiencies associated with relying exclusively on augmentations. While we motivate and emphasize the efficacy of our model based on VICReg (Bardes et al., 2021), our approach can be seamlessly integrated with other SSL methods simply by modifying their invariance terms through the exact process.

Graph Neural Networks (GNNs) have the inherent ability to capture label-related patterns due to the message-passing paradigm and the intrinsic characteristics of graph datasets. Hence, we construct a k-Nearest Neighbour (kNN) graph on the representations. Nodes in close proximity within the kNN graph exhibit a heightened likelihood of sharing the same label class. Therefore, this kNN graph serves as our first source to construct the compositional relation graph. PSEs, alongside the adjacency information, constitute our second primary source. Inspired by Lee et al. (2022), we employ the original input adjacency to construct a relation graph. Particularly in homophilic source graphs, adjacent nodes commonly share the same label class. Employing appropriate PSEs, transformers yield results comparable to message-passing networks. When a pair of points shares similar positional and structural properties, it indicates their overall similarity, offering auxiliary guidance for forming meaningful representations. Moreover, we incorporate a deep clustering algorithm rooted in the optimal transport (Asano et al., 2019) as the third source for guiding the invariance term. This module partitions the points into learnable clusters. Subsequently, we guide the model to create identical representations for points having similar soft clustering assignment distributions. This module is trained jointly in an end-to-end manner with the encoder, resembling an EM-style optimization approach in action, where both deep components evolve simultaneously, reflecting a dynamic interplay.

Two theoretical justifications support our proposal: the Laplacian Eigenmap (LE) perspective and the EM viewpoint. Firstly, adopting a spectral manifold learning perspective, the original solely augmentation-based VICReg objective can be formulated as an LE optimization (Balestriero & LeCum, 2022). The implicit augmentation-based relation graph results in disconnected islands corresponding to a rank deficiency of its Laplacian. We mitigate this through explicitly generating the relation graph, facilitating the connection of these islands. Secondly, SSL methods address an underlying two-step EM characterized by two implicit sets of variables (Chen & He, 2021). We distinctly and explicitly outline the representatives of these two steps. The Expectation step (E-step) leverages the learned representation to dynamically generate a relation graph, identifying candidates to promote similar representations. The Maximization step (M-step) refines the encoder by incorporating information from the determined relation graph. These two modules synergize, with the relation graph generator pinpointing candidate pairs for the invariance term and the encoder ensuring the enforcement of identical representation pairs. Our introduced objective function facilitates and stabilizes the joint optimization of these modules, enabling simultaneous execution of the two steps in a single gradient update. Following extensive experimentation across diverse graph datasets, we showcase the superior quality of the learned representation, consistently outperforming previous methods.

2 Related Work

2.1 Self-supervised Representation Learning

Contrastive SSL (Misra & Maaten, 2020; Bromley et al., 1994; Hjelm et al., 2019; Chen et al., 2020c; Hadsell et al., 2006; Ye et al., 2019; Wu et al., 2018; Chen et al., 2020b) constructs positive pairs employing data augmentation to push their representations closer while pulling apart the negative pairs utilizing InfoNCE (van den Oord et al., 2018). These pairs could be constructed on a mini-batch (Chen et al., 2020a) or employing memory banks (He et al., 2020). Clustering-based SSL (Bautista et al., 2016; Yang et al., 2016; Xie et al., 2016; Huang et al., 2019; Zhuang et al., 2019; Caron et al., 2019; Asano et al., 2019; Yan et al., 2020) employs a notion of clustering to form the representations by pseudo-labels (Caron et al., 2018) or enforcing identical clustering assignments of augmented pairs instead of directly enforcing identical features (Caron et al., 2020). Knowledge distillation-based SSL leverages student-teacher architectures (Hinton et al., 2015; Grill et al., 2020; Chen & He, 2021; Gidaris et al., 2021; Grill et al., 2020; Gidaris et al., 2020), employing an Exponential Moving Average encoder and a Stop-Gradient (SG) mechanism. Other works maximize the mutual information of representations (Ermolov et al., 2021; Zbontar et al., 2021). Notably, VICReg

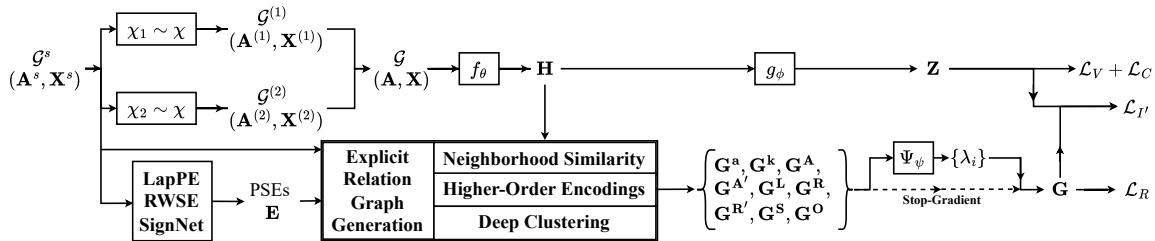


Figure 1: The comprehensive architecture of ExGRG. We incorporate augmented views $\mathcal{G}^{(1)}$ and $\mathcal{G}^{(2)}$ from source graph $\mathcal{G}^{(s)}$ to compose an input graph \mathcal{G} , which is then fed into encoder f_θ and expander g_ϕ to produce representations \mathbf{H} and embeddings \mathbf{Z} . We explicitly generate a compositional relation graph \mathbf{G} , aggregated from various intermediate relation graphs, to guide the invariance term $\mathcal{L}_{I'}$ instead of relying solely on augmentations.

(Bardes et al., 2021) decorrelates embedding dimensions to prevent preserving redundant information, and VICRegL (Bardes et al., 2022) employs local and global features, enforcing the invariance term for specific image patches.

2.2 Graph Representation Learning

GNNs (Kipf & Welling, 2016a; Veličković et al., 2017; Hamilton et al., 2017; Xu et al., 2018) accept node features and sufficient annotated data to form representations by recursively aggregating the neighbor’s information. Yet, to truly utilize the abundant unlabelled graph data, graph SSL pre-train GNNs to construct node- and graph-level representations without costly labels (García-Durán & Niepert, 2017; Kipf & Welling, 2016b; Bojchevski & Günnemann, 2017). Augmentation-based methods (You et al., 2020; Peng et al., 2020; Hassani & Khasahmadi, 2020; Zhu et al., 2021a;b; 2020c; Thakoor et al., 2021; Zhu et al., 2020b) encourage the representations to be invariant to a specifically designed graph transformation. A BERT-inspired method (Devlin et al., 2018; Hu et al., 2019) masks features of graphs with special structures. DGI (Veličković et al., 2018) aligns a local graph patch with the global one by maximizing the mutual information (Hjelm et al., 2019), followed by edge and node feature extensions (Peng et al., 2020; Jing et al., 2021) and tackling graph classification (Sun et al., 2019). Contrastive methods (Zhu et al., 2020c; 2021b; You et al., 2020; Hassani & Khasahmadi, 2020; Tian et al., 2020; Liu et al., 2023b) are generally inspired by SimCLR (Chen et al., 2020a), employing negative pairs resulting in the sampling bias issue (Bielak et al., 2021), meaning some negative samples may have similar semantics to the anchor while being pulled apart. PGCL (Lin et al., 2022) tackles the sampling bias, constructing the negative pairs from different clusters, while BGRL (Thakoor et al., 2021) adopts the non-contrastive BYOL (Grill et al., 2020).

AFGRL (Lee et al., 2022), an augmentation-free BYOL-based method, incorporates kNN, KMeans, and adjacency as local structures and global semantics. Similarly, SPGCL (Wang et al., 2023), an augmentation-free contrastive method, leverages kNN with a single encoder pass. We distinguish ourselves by offering a non-contrastive comprehensive framework. ExGRG generates and incorporates additional guidance in the form of relation graphs. We propose constructing an explicit compositional relation graph from various sources through a learnable aggregation mechanism. This relation graph identifies candidate pairs for the invariance term based on the theoretical connections between SSL, LE algorithm, and EM optimization. We stand out by introducing a novel approach leveraging PSEs in an unexplored context. ExGRG marks the pioneering attempt to employ a learnable clustering mechanism to drive the invariance term, departing from relying solely on augmentation.

3 Method

3.1 Preliminary

3.1.1 Graph SSL

As demonstrated in Fig. 1, the initial data points are M nodes within a source graph $\mathcal{G}^s = (\mathbf{A}^s, \mathbf{X}^s)$, where $\mathbf{A}^s \in \mathbb{R}^{M \times M}$ represents the adjacency and $\mathbf{X}^s \in \mathbb{R}^{M \times D_{in}}$ signifies the node features. In addition, $\mathbf{Y}^s \in \mathbb{R}^M$ denotes the node classification labels. Transformations χ_i are sampled from the distribution of data augmentations χ

to yield V views as $\mathcal{G}^{(i)} = (\mathbf{A}^{(i)}, \mathbf{X}^{(i)}) = \chi_i(\mathcal{G}^s)$, where $i \in \{1, \dots, V\}$, $\mathbf{A}^{(i)} \in \mathbb{R}^{M \times M}$, $\mathbf{X}^{(i)} \in \mathbb{R}^{M \times D_{in}}$, and typically $V=2$. The mini-batch graph $\mathcal{G} = (\mathbf{A}, \mathbf{X})$ is then constructed, where $\mathbf{A} \in \mathbb{R}^{N \times N}$ is the aggregation of adjacencies $\{\mathbf{A}^{(1)}, \dots, \mathbf{A}^{(V)}\}$, $\mathbf{X} = [\mathbf{X}^{(1)}; \dots; \mathbf{X}^{(V)}] \in \mathbb{R}^{N \times D_{in}}$, and $N = VM = 2M$ denotes the mini-batch size. This graph \mathcal{G} is subsequently fed into the graph encoder f_θ , which is usually a GNN. The representations $\mathbf{H} = f_\theta(\mathcal{G}) \in \mathbb{R}^{N \times D_H}$ produce embeddings $\mathbf{Z} = g_\phi(\mathbf{H}) \in \mathbb{R}^{N \times D_Z}$, employing the expander g_ϕ , interchangeably referred to as the projector or decoder in the literature, which is a Multi-Layer Perceptron (MLP).

The essence of SSL lies in employing signals inherent in data points as a form of supervision. SSL pre-training aims to discover representations of input points by identifying f_θ and g_ϕ . Subsequently, the pre-trained f_θ is utilized in downstream tasks, predicting \mathbf{Y}^s from \mathcal{G}^s , through linear probing, nonlinear probing, or fine-tuning. In linear probing, the prevailing approach in graph SSL, a single linear layer is affixed to the frozen pre-trained f_θ while detaching g_ϕ . This linear layer is trained for the downstream node classification task, utilizing the frozen representations as inputs. Though ExGRG centers around a node-level representation learning task, it can be seamlessly extended to learn graph- and link-level representations, with details provided in *Appendix § A.1*.

3.1.2 VICReg and Relation Graph

Contrastive SSL prevents the representation collapse by incorporating negative pairs (Chen et al., 2020a). In contrast, the VICReg objective \mathcal{L}_{vic} (Eq. 3) introduces constraints to maximize the volume of the embedding space through two regularization terms, variance \mathcal{L}_V and covariance \mathcal{L}_C (Eq. 1). The term \mathcal{L}_V ensures variance of embedding dimensions exceeds a threshold, while \mathcal{L}_C enforces decorrelation between every pair of dimensions. The invariance term \mathcal{L}_I (Eq. 2) encourages similar representations for semantically related points through augmentation.

$$\mathcal{L}_V = \sum_{k=1}^{D_Z} \max\left(0, 1 - \sqrt{\text{Cov}(\mathbf{Z})_{k,k}}\right), \quad (1)$$

$$\mathcal{L}_C = \sum_{k=1}^{D_Z} \sum_{j=1, j \neq k}^{D_Z} \text{Cov}(\mathbf{Z})_{k,j}^2.$$

$$\mathcal{L}_I = \sum_{(i,j) \in S_a} \|\mathbf{Z}_{i,\cdot} - \mathbf{Z}_{j,\cdot}\|_2^2 \quad (2)$$

$$\mathcal{L}_{vic} = \alpha \mathcal{L}_V + \beta \mathcal{L}_C + \gamma \mathcal{L}_I \quad (3)$$

The invariance term \mathcal{L}_I is exclusively guided by augmentations, performed on data points with index pairs (i, j) in an implicitly defined set $S_a = \{(i, j) \in \mathbb{N}^2 \mid \mathbf{X}_{i,\cdot}$ and $\mathbf{X}_{j,\cdot}$ are augmented from same source $\mathbf{X}_{k,\cdot}^s$, s.t. $1 \leq i < j \leq N$ and $1 \leq k \leq \frac{N}{2}\}$. The notation \mathbf{X} encompasses all points from both views within a unified matrix. Thus, with $(i, j) \in S_a$, the i -th point $\mathbf{X}_{i,\cdot}$ is the same as the k -th point in the first view, denoted as $\mathbf{X}_{k,\cdot}^{(1)}$. Similarly, the j -th point $\mathbf{X}_{j,\cdot}$ is the same as the k -th point in the second view, represented as $\mathbf{X}_{k,\cdot}^{(2)}$. The pair $(\mathbf{X}_{i,\cdot}, \mathbf{X}_{j,\cdot})$ is augmented from the same source point $\mathbf{X}_{k,\cdot}^s$. In the original invariance term \mathcal{L}_I , the enforcement is applied only over $(i, j) \in S_a$. We can conceptualize the relations among data points determined by this augmentation using a relation matrix $\mathbf{G}^a \in \mathbb{R}^{N \times N}$, where $\mathbf{G}_{i,j}^a = 1$ if $(i, j) \in S_a$, and $\mathbf{G}_{i,j}^a = 0$ otherwise. A relation matrix can be interpreted as an adjacency matrix for a relation graph, though we may use the terms *relation graph* and *relation matrix* interchangeably.

3.2 Explicit Compositional Relation Graph

Eq. 4 demonstrates the ExGRG’s invariance term $\mathcal{L}_{I'}$ employing our explicitly-generated compositional relation graph $\mathbf{G} \in \mathbb{R}^{N \times N}$ as opposed to only relying on augmentations \mathbf{G}^a . Our invariance term $\mathcal{L}_{I'}$ may be reduced to the original \mathcal{L}_I by simply setting $\mathbf{G} = \mathbf{G}^a$.

$$\mathcal{L}_{I'} = \sum_{i=1}^N \sum_{j=1}^N \mathbf{G}_{i,j} \|\mathbf{Z}_{i,\cdot} - \mathbf{Z}_{j,\cdot}\|_2^2 \quad (4)$$

Two theoretical justifications underpin the rationale behind explicitly generating \mathbf{G} . This is motivated by the interplay between SSL with (i) the LE method and (ii) the EM optimization.

3.2.1 Laplacian Eigenmap Perspective

In variance-covariance-constrained VICReg, $\alpha = \beta \gg \gamma$, signifying that the variance and covariance terms in \mathcal{L}_{Vic} are already satisfied (Eq. 3). Optimizing this VICReg objective is equivalent to solving the LE problem in *Appendix* Eq. 14 (Balestriero & LeCun, 2022). The distinction lies in VICReg’s \mathbf{G} being determined through data augmentations, while in LE, it can be designed by forming kNN graphs in the input. Due to the duality between S_a and G^a , the augmentation-based relation graph G^a consists of $M = \frac{N}{2}$ disconnected islands. Therefore, the corresponding Laplacian L^a for \mathbf{G}^a suffers from rank deficiency, as it has $\frac{N}{2}$ zero eigenvalues. In addition, due to the shortcomings of graph augmentations, connections between pairs of data points within each island in \mathbf{G}^a tend to be much less valuable compared to the vision domain. To address this challenge, we mitigate the rank deficiency of L^a by constructing a more informative \mathbf{G} through the incorporation of additional sources to guide the invariance term. We introduce meaningful entries to \mathbf{G} , establishing connections among the disconnected islands while assigning soft importance to each connection.

3.2.2 Alternating Two-Step EM Perspective

SimSiam (Chen & He, 2021) hypothesizes that SSL methods with Siamese architectures share an underlying optimization problem that could be effectively modeled employing the EM framework. In this optimization, SSL pre-training deals with two implicit sets of variables, reflecting an implied alternating optimization for each set in EM. Employing SG emerges as a viable approach to prevent collapse, resembling the alternating two-step EM optimization style in a single gradient update. The E-step is performed utilizing a predictor. Instead of directly comparing augmented views, the predictor assigns implicit targets for each anchor point, upon which the invariance loss is applied. In the M-step, the encoder is updated but only through one of the two available paths employing the SG technique.

ExGRG departs from computing these implicit targets. Instead, we opt for an explicit, end-to-end methodology that leverages nodes’ intrinsic information and characteristics to construct the relation graph. The connections in our relation graph determine candidate targets for each anchor point, formulated as the entries within \mathbf{G} . Within our framework, the two EM steps are consolidated into a single update via a joint optimization. Notably, ExGRG diverges from the implicit sets mentioned earlier. Instead, we utilize distinct and explicit sets of parameters. Specifically, leveraging our proposed loss function, both the parameters of the encoder and the relation graph generation modules are simultaneously updated.

In the EM algorithm, the E-step assigns data points to different given distributions. In ExGRG, this assignment corresponds to constructing \mathbf{G} , indicating which points should be brought closer. This E-step offers a roadmap for our M-step, which incorporates the invariance term $\mathcal{L}_{I'}$ based on the constructed \mathbf{G} . Optimizing $\mathcal{L}_{I'}$ leads to updating f_θ and g_ϕ , leading to new \mathbf{H} and \mathbf{Z} , which subsequently determine a new \mathbf{G} in the E-step of the next iteration.

3.2.3 Intra-view and Soft Relations

An invariance term $\mathcal{L}_{I'}$ based on constructing \mathbf{G} enables capturing and enforcing similarities among points within a view (intra-view) or across different views (inter-view). In essence, the enforcement of invariance criteria occurs concurrently for an anchor point in three key scenarios: **(i)** with its corresponding point in the other view, both resulting from augmentations on the same source, **(ii)** with its analogous points from the same view representing augmentations from different source points but sharing similar semantics to the anchor point, and **(iii)** with some analogous points from the other view holding similar characteristics as described in (ii). While conventional methods only support scenario (i), our extension enables us to integrate additional information from the same mini-batch.

Another distinction in our approach is the incorporation of support for soft values of relations. Unlike the binary nature of the conventional \mathbf{G}^a entries (0 or 1), we allow for soft values that indicate the degree of enforcing identical representations for a candidate pair in \mathbf{G} . This introduces flexibility and indicates the relative importance of each connection pair compared to other pairs resembling LE.

3.3 Strategies for Constructing Relation Graphs

Our approach to enhancing the invariance term involves exploring ways to construct more informative relation graphs. This empowers the invariance term to leverage additional similarities beyond augmentations through

(i) utilizing *Neighborhood Similarity* employing the kNN graph, (ii) exploiting *Higher-Order Encodings* as the structural and positional similarities of nodes, and (iii) incorporating an end-to-end *Deep Clustering* algorithm.

3.3.1 Neighborhood Similarity in the Representation Space

We can explicitly determine a relation graph by leveraging the similarities between the representations of points. This approach encourages the convergence of embeddings for points with similar neighborhoods in the representation space, resembling LE. Thus, we compare the points in \mathbf{H} to compute the kNN relation matrix denoted by $\mathbf{G}^k = F_k(\mathbf{G}^H) \in \mathbb{R}^{N \times N}$, where $\mathbf{G}_{i,j}^H = \text{sim}(\mathbf{H}_{i,\cdot}, \mathbf{H}_{j,\cdot})$ and $i, j \in \{1, \dots, N\}$. The function *sim* represents a notion of similarity, such as Euclidean or cosine similarity. Additionally, F_k sets entries other than the k -largest values in each row of its input to zero, resembling the kNN algorithm.

3.3.2 Higher-Order Graph Encodings

In homophilic input graphs, the proximity of two nodes in \mathcal{G}^s indicates sharing the same class label in \mathbf{Y}^s (Zhu et al., 2020a). Therefore, depending on the degree of homophily in the source graph \mathcal{G}^s , the edges between source points in \mathbf{A}^s can be exploited to construct an informative relation matrix $\mathbf{G}^A = F_A(\mathbf{A}^s) \in \mathbb{R}^{N \times N}$, where F_A extracts the adjacency information corresponding to the N points in the mini-batch. Recognizing that \mathbf{G}^k or \mathbf{G}^A are often noisy on their own (Lee et al., 2022), we propose another more conservative filtered version through element-wise multiplication as $\mathbf{G}^{A'} = \mathbf{G}^A \odot \mathbf{G}^k$. This $\mathbf{G}^{A'}$ retains the soft similarities of \mathbf{G}^k , with additional details provided in *Appendix § A.5*.

Additionally, drawing inspiration from LE, we can conduct pre-processing on the input to extract characteristics that can be utilized to construct a more informative \mathbf{G} . This could involve leveraging the comparison of some statistics and features at the level of individual nodes, neighborhoods, or sub-graphs. To achieve this, we incorporate positional or structural similarities of nodes. Our approach differs from their typical application in transformers to enhance the identifiability of nodes within a graph (Liu et al., 2023a). To the best of our knowledge, this is the first attempt to integrate PSEs into the SSL pre-training.

Positional Encodings (PEs) attempt to encode the position of a node within a graph. Thus, comparing these encodings can help identify nodes with similar positions in the graph, capturing a higher-level understanding of what the adjacency matrix can signify. Alternatively, Structural Encodings (SEs) capture the structural characteristics of the neighboring region surrounding each node. By incorporating SEs, ExGRG gains access to rich information about nodes with analogous local and global connectivity patterns. Our approach encompasses three PSEs: Laplacian Eigenvectors Positional Encoding (LapPE) (Dwivedi et al., 2023), Random Walk Structural Encodings (RWSE) (Dwivedi et al., 2021), and SignNet (Lim et al., 2022). LapPE serves as a global PE, offering insights into the node’s overall position within the graph. RWSE provides local structural information, indicating the sub-structure to which a node belongs. SignNet, acting as another global positional encoder, is also capable of capturing some local structural information.

To construct a relation matrix from these PSEs, a comparison of encodings for pairs of nodes is necessary, followed by the formation of candidate pairs based on a construction algorithm such as kNN. By denoting a computed PSE as $\mathbf{E} \in \mathbb{R}^{N \times D_E}$, we obtain $\mathbf{G}^{PSE} = F_k(\mathbf{G}^E) \in \mathbb{R}^{N \times N}$, where $\mathbf{G}_{i,j}^E = \text{sim}(\mathbf{E}_{i,\cdot}, \mathbf{E}_{j,\cdot})$ and $i, j \in \{1, \dots, N\}$. By incorporating LapPE, RWSE, and SignNet PSEs into the \mathbf{G}^{PSE} placeholder, we construct three relation matrices, \mathbf{G}^L , \mathbf{G}^R , and \mathbf{G}^S . Similar to $\mathbf{G}^{A'}$, we observe the filtered RWSE $\mathbf{G}^{R'} = \mathbf{G}^R \odot \mathbf{G}^k$ to be more beneficial for certain datasets.

3.3.3 Deep Clustering for Relation Graph Generation

Various methods are introduced to jointly optimize a deep feature extractor module and a deep clustering module (Zhou et al., 2022). Conventionally, this is performed by leveraging the feature extractor module to provide essential features for the clustering module, with the aim of addressing *a clustering task*. However, in our approach, we invert this paradigm by proposing a novel relation between these two modules through our introduced objective function. Instead, we leverage the clustering module to explicitly guide the feature extractor module towards *a representation learning task*.

Our encoder and learnable clustering modules collaboratively aim to enhance the representations. The clustering module employs learnable prototypes to assign a probability distribution to each data point. This distribution indicates the confidence of assigning a data point to different clusters. Subsequently, these assignments are

employed to guide the invariance loss. This encourages the encoder to map points with similar clustering assignments to identical representations. Both the prototypes and the encoder are learned jointly, providing a more integrated and effective approach.

This marks a novel attempt to integrate a learnable clustering algorithm for representation learning. While a clustering algorithm is previously employed in SSL methods to partition the points (Caron et al., 2020), a key distinction lies in the representation learning aspect. In these methods, the invariance loss is still guided through data augmentation. This means that for points in S_a , instead of ensuring identical features directly through \mathcal{L}_I , they aim for identical clustering assignments. In contrast, ExGRG positions the clustering module as an explicit and direct guide, promoting the same representation for data points with similar cluster assignments at each iteration. In essence, our proposal deviates from the approach of enforcing identical cluster assignments for augmentation-based paired points; instead, we enforce identical representations for points with similar cluster assignments. The candidate pairs for this enforcement encompass the entire mini-batch, not only pairs augmented from the same source.

In our deep clustering module, we leverage optimal transport (Asano et al., 2019) to partition the points employing K trainable prototypes $\mathbf{C} \in \mathbb{R}^{K \times D_H}$. The probabilities $\mathbf{P} \in \mathbb{R}^{N \times K}$, represent the distribution of assignments of points to different clusters. They are computed by comparing the representations \mathbf{H} with prototypes \mathbf{C} , followed by a softmax function with temperature τ . The probability $P_{j,k}$ of assigning the point $\mathbf{H}_{j,\cdot} \in \mathbb{R}^{D_H}$ to the k -th prototype $\mathbf{C}_{k,\cdot} \in \mathbb{R}^{D_H}$ is given by

$$P_{j,k} = \frac{\exp(\frac{1}{\tau} \mathbf{H}_{j,\cdot}^T \mathbf{C}_{k,\cdot})}{\sum_{k'} \exp(\frac{1}{\tau} \mathbf{H}_{j,\cdot}^T \mathbf{C}_{k',\cdot})}. \quad (5)$$

To update \mathbf{P} , we aim to make them more similar to codes $\mathbf{Q} \in \mathbb{R}^{N \times K}$, which serve as a refined version of \mathbf{P} computed from the optimal transport problem. The underlying concept of the target probability distribution \mathbf{Q} is evenly distributing data points among clusters. The updates for \mathbf{P} and \mathbf{C} are performed leveraging our loss term \mathcal{L}_O that aligns \mathbf{P} and \mathbf{Q} using cross-entropy for all pairs in S_O as

$$\mathcal{L}_O = \frac{1}{|S_O|} \sum_{(i,j) \in S_O} l_{i,j}, \text{ where } l_{i,j} = - \sum_k \mathbf{Q}_{i,k} \log \mathbf{P}_{j,k}, \quad (6)$$

$$\text{and } S_O = \{(i,j) \in \mathbb{N}^2 \mid i=j\} \cup S_a. \quad (7)$$

At each iteration, \mathbf{Q} is derived directly from \mathbf{C} and \mathbf{H} employing the Sinkhorn-Knopp algorithm (Cuturi, 2013; Asano et al., 2019; Caron et al., 2020), with further details provided in *Appendix* § A.6. Simultaneously, \mathbf{P} is aligned with \mathbf{Q} to adjust \mathbf{C} accordingly for the subsequent iterations. To incorporate the auxiliary online extracted information available in \mathbf{P} , a relation matrix $\mathbf{G}^O \in \mathbb{R}^{N \times N}$ is constructed as

$$\mathbf{G}^O = F_K(F_n(\mathbf{G}^P)), \text{ where } \mathbf{G}_{i,j}^P = \sum_k \mathbf{P}_{i,k} \log \mathbf{P}_{j,k}. \quad (8)$$

Here, F_n normalizes entries of \mathbf{G}^P to $[0,1]$. Additionally, F_K selects the top K_g entries of the input matrix globally and sets the rest to zero. As a result, \mathbf{G}^O is a sparse normalized version of \mathbf{G}^P . The entry $\mathbf{G}_{i,j}^P$ represents negative cross-entropy over distributions $\mathbf{P}_{i,\cdot}$ and $\mathbf{P}_{j,\cdot}$, indicating a notion of similarity for clustering assignments. If points $\mathbf{H}_{i,\cdot}$ and $\mathbf{H}_{j,\cdot}$ share high similarity in their clustering assignments, signifying similar characteristics, their representations are encouraged to be closer through \mathbf{G}^O .

3.4 Multi-Source Aggregation

To compute the invariance term $\mathcal{L}_{I'}$ (Eq. 4), we construct a compositional relation matrix \mathbf{G} through aggregating various relation matrices $\mathbf{G}^{(i)} \in S_G$ derived from previously-discussed sources gathered in S_G (Eq. 10). In a straightforward scenario, this aggregation can be accomplished through summation with learnable coefficients λ_i . This is illustrated in Eq. 9, where F_{SG} denotes the identity function but enforces the SG mechanism outlined in § 3.5. Combining Eq. 9 and Eq. 4, we observe that this effective aggregation can also be represented as

individual invariance terms corresponding to each of the $\mathbf{G}^{(i)} \in S_G$. Besides, employing a softmax, we ensure λ_i are normalized, guaranteeing that they collectively sum up to one, i.e., we enforce $\sum_{\mathbf{G}^{(i)} \in S_G} \lambda_i = 1$.

$$\mathbf{G} = \sum_{\mathbf{G}^{(i)} \in S_G} \lambda_i F_{SG}(\mathbf{G}^{(i)}), \quad (9)$$

$$\text{where } S_G = \{\mathbf{G}^a, \mathbf{G}^k, \mathbf{G}^A, \mathbf{G}^{A'}, \mathbf{G}^L, \mathbf{G}^R, \mathbf{G}^{R'}, \mathbf{G}^S, \mathbf{G}^O\}. \quad (10)$$

To generate the learnable coefficients λ_i , we employ an MLP Ψ_ψ as a hypernetwork (Ha et al., 2016). This aims to efficiently aggregate an arbitrary number of relation graphs using a single module in an online manner. We leverage a hypernetwork-inspired formulation for its computational capabilities encompassing information-sharing, compressed nature, and expedited training process (Chauhan et al., 2023). This module receives some characteristics about each $\mathbf{G}^{(i)} \in S_G$ in an online manner as

$$\lambda_i = \Psi_\psi \left(F_s(\mathbf{G}^{(i)}) \right), \quad (11)$$

where F_s denotes a function that computes two simple yet effective statistics from its input $\mathbf{G}^{(i)}$ to determine the appropriate contribution to \mathbf{G} : (i) the sum of $\mathbf{G}^{(i)}$ entries, reflecting the average strength of connections within $\mathbf{G}^{(i)}$, and (ii) the count of $\mathbf{G}^{(i)}$ non-zero entries, resembling the level of sparsity.

3.5 End-to-End Training Procedure

The transition between optimizing our modules, specifically the alteration of (i) updating f_θ and g_ϕ , and (ii) generation of a more informative $\mathbf{G}^{(i)} \in S_G$ and eventually \mathbf{G} , can be achieved through the incorporation of an SG mechanism (Eq. 9), inspired by Grill et al. (2020) and Chen & He (2021), alongside a relation matrix regularization as

$$\mathcal{L}_R = - \sum_{i,j} (\mathbf{G}_{i,j})^2. \quad (12)$$

These two components are introduced to prevent $\mathbf{G}^{(i)}$ and \mathbf{G} from collapsing to a degenerate solution, wherein all entries are encouraged to be zero under the influence of \mathcal{L}_R . This integration enables us to squeeze the two EM steps into a single gradient update, thus enabling joint optimization. This strategy aims to enhance the synergy between the encoder’s parameter adjustment and the refinement of the informative content within the relation matrices. Additional details are provided in *Appendix § A.7*.

Finally, to facilitate end-to-end training of our model through gradient descent, we employ a comprehensive multi-term loss function \mathcal{L}_{ETE} that encompasses the terms discussed so far as

$$\mathcal{L}_{ETE} = \alpha \mathcal{L}_V + \beta \mathcal{L}_C + \gamma \mathcal{L}_I + \alpha_1 \mathcal{L}_O + \alpha_2 \mathcal{L}_R, \quad (13)$$

where α , β , and γ , α_1 and α_2 serve as coefficients for the respective loss terms.

4 Experimental Evaluation

4.1 Experimental Setup

We undertake an extensive experimental analysis, aiming to demonstrate the efficacy of our approach and its superiority in comparison to other state-of-the-art methods. A GCN (Kipf & Welling, 2016a) as the encoder f_θ is utilized, with details provided in *Appendix § B.2*. Also, we follow the linear probing protocol, the established approach in prior graph SSL works (Thakoor et al., 2021). Further details can be found in § 3.1.1 and *Appendix § B.3*.

Datasets: We employ a wide range of real-world graphs within 9 node classification datasets, including WikiCS, Amazon Computers (AmzComp), Amazon Photo (AmzPhoto), Coauthor CS (CoCS), Coauthor Physics (CoPhy), Cora, CiteSeer, PubMed, and DBLP, with corresponding statistics in *Appendix Table 3*.

Table 1: Downstream performance measured in terms of node classification accuracy’s mean and standard deviation over 20 random model initializations and dataset splits. *OOM* indicates Out Of Memory.

Model	WikiCS	AmzComp	AmzPhoto	CoCS	CoPhy	Cora	CiteSeer	PubMed	DBLP
Supervised MLP	71.98±0.42	73.81±0.21	78.53±0.32	90.37±0.19	93.58±0.41	47.92±0.41	49.31±0.26	69.14±0.34	-
Supervised GCN	77.19±0.12	86.51±0.54	92.42±0.22	93.03±0.31	95.65±0.16	81.54±0.68	70.73±0.65	79.16±0.25	82.7±0.00
Node2Vec	71.79±0.05	84.39±0.08	89.67±0.12	85.08±0.03	91.19±0.04	71.08±0.91	47.34±0.84	66.23±0.95	-
DeepWalk	74.35±0.06	85.68±0.06	89.44±0.11	84.61±0.22	91.77±0.15	70.72±0.63	51.39±0.41	73.27±0.86	-
DW + Features	77.21±0.03	86.28±0.07	90.05±0.08	87.70±0.04	94.90±0.09	-	-	-	-
DGI	75.35±0.14	83.95±0.47	91.61±0.22	92.15±0.63	94.51±0.52	82.34±0.71	71.83±0.54	76.78±0.31	-
GMI	74.85±0.08	82.21±0.31	90.68±0.17	OOM	OOM	82.39±0.65	71.72±0.15	79.34±1.04	-
MVGRL	77.52±0.08	87.52±0.11	91.74±0.07	92.11±0.12	95.33±0.03	83.45±0.68	73.28±0.48	80.09±0.62	-
GRACE	77.97±0.63	86.50±0.33	92.46±0.18	92.17±0.04	OOM	81.92±0.89	71.21±0.64	80.54±0.36	-
GCA	77.94±0.67	87.32±0.50	92.39±0.33	92.84±0.15	OOM	82.07±0.10	71.33±0.37	80.21±0.39	-
BGRL	79.98±0.10	90.34±0.19	93.17±0.30	93.31±0.13	95.73±0.05	83.83±1.61	72.32±0.89	86.03±0.33	84.07±0.23
AFGRL	77.62±0.49	89.88±0.33	93.22±0.28	93.27±0.17	95.69±0.10	81.60±0.54	71.02±0.37	80.02±0.48	-
SPGCL	79.01±0.51	89.68±0.19	92.49±0.31	91.92±0.10	95.12±0.15	83.16±0.13	71.96±0.42	79.16±0.73	-
ExGRG	82.09±0.67	93.37±0.48	96.42±0.54	94.57±0.31	96.59±0.20	97.87±0.55	89.68±1.46	88.03±0.49	86.01±0.59

Baselines: We compare ExGRG with various graph representation learning methods, encompassing (i) supervised MLP employing raw node features and GCN (Kipf & Welling, 2016a), (ii) conventional unsupervised graph embedding works Node2Vec (Grover & Leskovec, 2016) and DeepWalk (Perozzi et al., 2014), alongside (iii) state-of-the-art contrastive and non-contrastive SSL methods, including DGI (Veličković et al., 2018), GMI (Peng et al., 2020), MVGRL (Hassani & Khasahmadi, 2020), GRACE (Zhu et al., 2020c), GCA (Zhu et al., 2021b), BGRL (Thakoor et al., 2021), and augmentation-free works AFGRL (Lee et al., 2022) and SPGCL (Wang et al., 2023).

4.2 Experimental Results

The empirical performance compared to the baselines is presented in Table 1, showcasing node classification accuracy’s mean and standard deviation over 20 trials. Each trial corresponds to a random model initialization and distinct train-validation-test splits. Data for other methods are sourced from previous works where available (Thakoor et al., 2021; Lee et al., 2022; Wang et al., 2023). ExGRG consistently outperforms all baselines across these datasets. This demonstrates the effectiveness of our proposed framework in explicitly generating relation graphs by incorporating various forms of prior knowledge, such as PSEs and adjacency, as well as online extracted information through a kNN graph and a deep clustering module. Concerning Table 1, the following insights are noteworthy.

(i) Previous SSL methods consistently outperform supervised GCN with a notable gap across all datasets except the large-scale ones CoCS and CoPhy, where the top-performing method, BGRL, achieves comparable results with GCN. However, ExGRG maintains superiority even under this scenario. (ii) When comparing MLP with GCN, the performance gap is more pronounced in Cora and CiteSeer compared to CoCS and CoPhy, underscoring the importance of graph structural properties facilitated by the message-passing mechanism. This trend aligns with the datasets where the ExGRG’s most significant improvements are observed compared to the state-of-the-art. This indicates the effectiveness of incorporating adjacency and PSEs into the learning process through their corresponding relation graphs. (iii) Despite the limitations of graph augmentations, comparing the two BYOL-based methods, BGRL with the augmentation-free AFGRL across WikiCS, AmzComp, Cora, CiteSeer, and PubMed, we observe the superiority of employing graph augmentations. This validates our approach of not solely relying on augmentations while still utilizing them in G^a alongside other informative sources.

(iv) The significance of our non-contrastive approach is highlighted in PubMed, where BGRL, the other non-contrastive work, also outperforms contrastive approaches GRACE, GCA, and SPGCL by a considerable margin. We hypothesize that contrastive methods suffer from the sampling bias issue in such scenarios, where the representation of every other point is treated as negative samples to be pushed apart from the anchor. In contrast, we adopt volume maximization terms \mathcal{L}_V and \mathcal{L}_C alongside explicitly determining which points should be connected in our compositional relation graph, leading to identical representations in \mathcal{L}_V . (v) Contrastive approaches also face significant memory consumption due to the excessive number of negative pairs, making them incapable of handling large-scale datasets like CoCS and CoPhy. Conversely, our non-contrastive approach manages to outperform even with a small mini-batch size N , as demonstrated in *Appendix* Fig. 11.

Table 2: Ablation studies on Amazon Computers. Models are altered concerning ExGRG (5k iters) as the reference. The metrics are outlined in *Appendix § B.4*.

[Ablated] Model	Accuracy	corr H	corr Z	std H	std Z	nstd H	rank H	rank Z
ExGRG (9k iters)	93.37 ± 0.48	0.0025	0.1072	0.1536	0.9185	0.0447	512	1024
ExGRG (5k iters)	93.26 ± 0.57	0.0009	0.0866	0.1250	0.6769	0.0448	512	1024
Binary G	93.21 ± 0.40	142.28	0.0012	0.7460	0.0985	0.0413	279	777
No \mathcal{L}_R	92.89 ± 0.50	5513.5	0.0001	1.5969	0.0222	0.0378	19	272
No Ψ_ψ	92.90 ± 0.52	5514.3	0.0001	1.5971	0.0223	0.0378	19	269
No F_{SG} on G^S	93.12 ± 0.51	0.0009	0.0825	0.1200	0.6726	0.0448	512	1024
Add Standalone G^k	91.67 ± 0.47	0.0006	0.0485	0.1127	0.4813	0.0439	512	1024
No $G^{A'}$ or $G^{R'}$	93.11 ± 0.47	0.0010	0.0544	0.1200	0.5708	0.0448	512	1024
No G^a	93.03 ± 0.52	0.0010	0.0550	0.1202	0.5768	0.0448	512	1024
No $G^{A'}$	93.03 ± 0.53	0.0010	0.0550	0.1202	0.5768	0.0448	512	1024
No G^L	92.96 ± 0.58	0.0007	0.0778	0.1161	0.6552	0.0448	512	1024
No $G^{R'}$	92.94 ± 0.47	4348.2	0.0001	1.5292	0.0224	0.0374	23	294
G^R instead of $G^{R'}$	92.89 ± 0.61	0.0043	0.0602	0.1326	0.4390	0.0446	512	1024
No G^S	93.15 ± 0.53	0.0011	0.0729	0.1227	0.6525	0.0448	512	1024
No G^{PSE} or $G^{A'}$	93.04 ± 0.49	0.0007	0.0780	0.1167	0.6568	0.0448	512	1024
No G^O	92.82 ± 0.56	4519.4	0.0001	1.5336	0.0217	0.0346	22	297
F_k instead of F_K in G^O	93.12 ± 0.51	0.0009	0.0825	0.1200	0.6726	0.0448	512	1024
$S_O = \{(i,j) \mid i=j\}$	93.12 ± 0.51	0.0009	0.0825	0.1200	0.6726	0.0447	512	1024
$S_O = S_a$	93.12 ± 0.51	0.0009	0.0825	0.1200	0.6726	0.0448	512	1024
Intra Relations	93.26 ± 0.54	0.0027	0.1064	0.1524	0.9322	0.0321	512	1024

4.3 Ablation Studies

To showcase the effectiveness of our design choices and underscore the significance of each introduced component and loss term in \mathcal{L}_{ETE} , we conduct ablation studies on AmzComp (Table 2), alongside CiteSeer and Cora (*Appendix* Tables 4 and 5). We follow a similar 20-trial setup in the ablation studies and conduct these experiments with 5k pre-training iterations, with further details provided in § B.5. Our ablations yield the following insights.

(i) Utilizing a binary G , the prevalent approach in SSL, leads to a dimensional collapse in our framework, characterized by low feature spreads, diminished ranks, and elevated inter-feature correlations. This stems from the strict enforcement of either identical representations for a pair or none at all. However, we address this by employing finer enforcement in invariance term \mathcal{L}_I through soft G entries. (ii) Omitting regularization \mathcal{L}_R leads to the relation graph converging towards a degenerate solution where all G entries collapse to zero. Consequently, no guidance is provided for the invariance term, resulting in dimensional collapse and markedly reduced feature spread. (iii) Absence of Ψ_ψ results in dimensional collapse with low spreads. This occurs because the aggregation of various relation graphs remains fixed throughout training, employing λ_i in Eq. 9 as hyperparameters. We mitigate this issue by proposing online aggregation through Eq. 11. (iv) The SG mechanism prevents $G^{(i)} \in S_G$ and G from collapsing to a degenerate solution, as demonstrated in Cora.

(v) Utilizing a standalone G^k results in extremely noisy over-enforcement of neighborhood proximities, leading to representations becoming excessively close, as evidenced by low spread for AmzComp and complete collapse in Cora. (vi) Augmentations in G^a prove to be extremely beneficial for Cora and CiteSeer, contradicting the adoption of a completely augmentation-free approach.

(vii) In AmzComp, removing G^a , $G^{A'}$, G^L , or G^S maintains full-rank representations with sufficient spread. Though accuracy slightly drops, we speculate that online clustering compensates for this absence to some extent. The information extracted in G^O can effectively provide some insights comparable to augmentations, adjacency, and PEs. Notably, G^O proves to be the most impactful among other relation graphs in AmzComp, enabling an

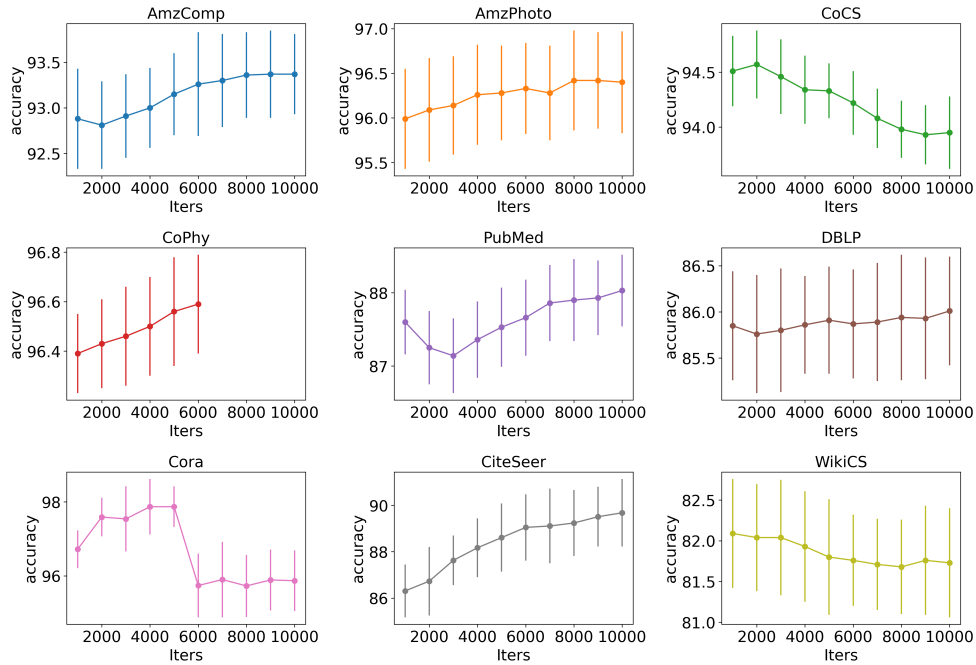


Figure 2: Accuracy vs. iterations over 20 trials throughout the SSL pre-training.

automatic online approach to capture information that other sources may also offer. This underscores our model’s capability to handle various scenarios where higher-order encodings may not be as useful, such as extremely sparse graphs. **(viii)** In AmzComp, the model collapses when we eliminate SE G^R , while still incorporating adjacency and PEs. We speculate that RWSE is particularly effective in mitigating noisy information from adjacency and PEs. Consequently, adjacency and PEs should be utilized in conjunction with SEs, leading to our proposal of employing PSEs as the higher-order encodings. Consistent with this rationale, eliminating the higher-order encodings entirely results in generally better performance than removing only one PSE at a time. **(ix)** The noisy nature of G^R is evident in CiteSeer, highlighting the effectiveness of filtering it to construct G^R .

(x) The profound impact of deep clustering in preventing collapse is evident. Our online clustering maintains a global perspective by evenly distributing representations to learnable prototypes, effectively mitigating potential over-enforcement caused by other relation graphs. **(xi)** Similarly, adopting a global perspective to sparsify G^O yields slightly improved performance. Utilizing the global F_K instead of the local F_k enables the model to capture a broader picture rather than focusing solely on local properties possibly covered by other relation graphs. **(xii)** Enforcing all relation graphs to consider intra-view relations alongside inter-view ones leads to convergence of spread to 1 in fewer iterations and even better downstream performance in Cora, although with a computational overhead.

4.4 SSL Pre-Training Analysis

SSL models undergo pre-training for a specific number of iterations before finally being evaluated on a downstream task. However, it is beneficial to examine the pre-training process periodically to gain insights into learning suitable representations. Thus, we evaluated checkpoints at intervals of 1k iterations. Due to the considerably higher resource consumption of CoPhy, pre-training is manually terminated before reaching 7k iterations.

Fig. 2 demonstrates the accuracy mean and standard deviation throughout the learning process. The general trend indicates that as the pre-training progresses, the representations tend to become more suitable for the downstream task, prominently observed in AmzComp, AmzPhoto, CoPhy, PubMed, DBLP, CiteSeer, and the initial iterations of CoCS and Cora. Notably, WikiCS exhibits a consistent accuracy for the first few thousand iterations, followed by a decline. In SSL training, the objective may not always align directly with the particular downstream task,

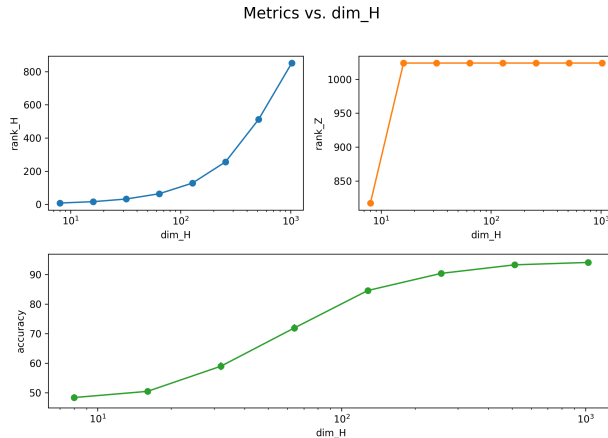


Figure 3: Impact of altering D_H on ranks and downstream accuracy for Amazon Computers.

as the goal is to derive a more generalized representation adaptable to various downstream tasks. Hence, the decreasing trends after a point suggest that ExGRG may sacrifice some aspects of a representation suitable for the specific node classification to enhance other aspects targeted in \mathcal{L}_{ETE} . Additionally, the overall decreasing trends for correlations, along with the prevailing increasing trends for standard deviations and ranks for both \mathbf{H} and \mathbf{Z} throughout the pre-training are detailed in *Appendix* Fig.4-9 and § B.6.

4.5 Hyperparameter Analysis

The employed hyperparameters, encompassing design choices and optimizers for each dataset, are outlined in *Appendix* Table 6 and § B.7. Here, we analyze the influence of these parameters on our model’s performance, focusing on AmzComp. Notably, Fig. 3 alters D_H , the number of feature dimensions of representations. Both accuracy and rank of \mathbf{H} exhibit an upward trend, indicating the model’s capacity to effectively leverage the feature dimensions to encode valuable information.

Furthermore, the impact of various parameters is detailed in *Appendix* Fig. 10-14 and § B.8. Notably, the simultaneous increase in both D_Z and D_H results in an ascending trend in accuracy and ranks, affirming the model’s effectiveness in leveraging larger feature dimensions. Conversely, alternative contrastive methods rapidly saturate, suffering from the curse of dimensionality (Zbontar et al., 2021). In addition, the model exhibits robustness concerning mini-batch size N , indicating its ability to derive meaningful directions for guiding the invariance term even with a reduced number of points. Moreover, the influence of k in \mathbf{G}^k reveals that extremely high k for kNN negatively impacts performance, contributing to heightened noise in guiding the invariance term. Also, increasing K in \mathbf{G}^O emphasizes the stability, but with an overall slightly increasing trend for downstream accuracy. Though we effectively leverage a higher number of prototypes, determining the appropriate number of clusters for each dataset is traditionally challenging (Zhou et al., 2022), underscoring the importance of achieving this general robustness.

5 Conclusion

In this paper, we introduced ExGRG, a novel graph SSL approach inspired by the theoretical interplay among the SSL pre-training approaches, the spectral embedding methods in manifold learning, and the EM optimization algorithm. ExGRG offers a comprehensive framework for injecting higher-order domain knowledge into the SSL process. This involves diverse forms of prior knowledge, including positional and structural encodings and adjacency, alongside online extracted information through a kNN graph and a deep clustering module. To achieve this, we propose explicitly generating a compositional relation graph to guide the invariance objective, deviating from the conventional reliance on data augmentations, which proves problematic and counter-intuitive in the context of the graph domain. Extensive experimental evaluations across diverse graph datasets showcase the superiority of ExGRG over state-of-the-art graph SSL approaches.

References

- Yuki Markus Asano, Christian Rupprecht, and Andrea Vedaldi. Self-labelling via simultaneous clustering and representation learning. *arXiv preprint arXiv:1911.05371*, 2019.
- Randall Balestriero and Yann LeCun. Contrastive and non-contrastive self-supervised learning recover global and local spectral embedding methods. *arXiv preprint arXiv:2205.11508*, 2022.
- Adrien Bardes, Jean Ponce, and Yann LeCun. Vicreg: Variance-invariance-covariance regularization for self-supervised learning. *arXiv preprint arXiv:2105.04906*, 2021.
- Adrien Bardes, Jean Ponce, and Yann LeCun. Vicregl: Self-supervised learning of local visual features. *arXiv preprint arXiv:2210.01571*, 2022.
- Miguel A. Bautista, Arsiom Sanakoyeu, Ekaterina Sutter, and Björn Ommer. Cliqecnn: Deep unsupervised exemplar learning. In *NeurIPS*, 2016.
- Piotr Bielak, Tomasz Kajdanowicz, and Nitesh V Chawla. Graph barlow twins: A self-supervised representation learning framework for graphs. *arXiv preprint arXiv:2106.02466*, 2021.
- Aleksandar Bojchevski and Stephan Günnemann. Deep gaussian embedding of graphs: Unsupervised inductive learning via ranking. *arXiv preprint arXiv:1707.03815*, 2017.
- Jane Bromley, Isabelle Guyon, Yann LeCun, Eduard Sackinger, and Roopak Shah. Signature verification using a “siamese” time delay neural network. In *NeurIPS*, 1994.
- Mathilde Caron, Piotr Bojanowski, Armand Joulin, and Matthijs Douze. Deep clustering for unsupervised learning. In *ECCV*, 2018.
- Mathilde Caron, Piotr Bojanowski, Julien Mairal, and Armand Joulin. Unsupervised pre-training of image features on non-curated data. In *ICCV*, 2019.
- Mathilde Caron, Ishan Misra, Julien Mairal, Priya Goyal, Piotr Bojanowski, and Armand Joulin. Unsupervised learning of visual features by contrasting cluster assignments. *Advances in neural information processing systems*, 33:9912–9924, 2020.
- Vinod Kumar Chauhan, Jiandong Zhou, Ping Lu, Soheila Molaei, and David A Clifton. A brief review of hypernetworks in deep learning. *arXiv preprint arXiv:2306.06955*, 2023.
- Ting Chen, Simon Kornblith, Mohammad Norouzi, and Geoffrey Hinton. A simple framework for contrastive learning of visual representations. In *International conference on machine learning*, pp. 1597–1607. PMLR, 2020a.
- Ting Chen, Simon Kornblith, Kevin Swersky, Mohammad Norouzi, and Geoffrey Hinton. Big self-supervised models are strong semi-supervised learners. In *NeurIPS*, 2020b.
- Xinlei Chen and Kaiming He. Exploring simple siamese representation learning. In *Proceedings of the IEEE/CVF conference on computer vision and pattern recognition*, pp. 15750–15758, 2021.
- Xinlei Chen, Haoqi Fan, Ross Girshick, and Kaiming He. Improved baselines with momentum contrastive learning. *arXiv preprint arXiv:2003.04297*, 2020c.
- Djork-Arné Clevert, Thomas Unterthiner, and Sepp Hochreiter. Fast and accurate deep network learning by exponential linear units (elus). *arXiv preprint arXiv:1511.07289*, 2015.
- Marco Cuturi. Sinkhorn distances: Lightspeed computation of optimal transport. *Advances in neural information processing systems*, 26, 2013.
- Jacob Devlin, Ming-Wei Chang, Kenton Lee, and Kristina Toutanova. Bert: Pre-training of deep bidirectional transformers for language understanding. *arXiv preprint arXiv:1810.04805*, 2018.
- Vijay Prakash Dwivedi, Anh Tuan Luu, Thomas Laurent, Yoshua Bengio, and Xavier Bresson. Graph neural networks with learnable structural and positional representations. *arXiv preprint arXiv:2110.07875*, 2021.

-
- Vijay Prakash Dwivedi, Chaitanya K Joshi, Anh Tuan Luu, Thomas Laurent, Yoshua Bengio, and Xavier Bresson. Benchmarking graph neural networks. *Journal of Machine Learning Research*, 24(43):1–48, 2023.
- Aleksandr Ermolov, Aliaksandr Siarohin, Enver Sangineto, and Nicu Sebe. Whitening for self-supervised representation learning. In *International Conference on Machine Learning*, pp. 3015–3024. PMLR, 2021.
- Alberto García-Durán and Mathias Niepert. Learning graph representations with embedding propagation. In *Neural Information Processing Systems*, 2017. ISBN 9781510860964.
- Spyros Gidaris, Andrei Bursuc, Nikos Komodakis, Patrick Pérez, and Matthieu Cord. Learning representations by predicting bags of visual words. In *CVPR*, 2020.
- Spyros Gidaris, Andrei Bursuc, Gilles Puy, Nikos Komodakis, Matthieu Cord, and Patrick Pérez. Online bag-of-visual-words generation for unsupervised representation learning. In *CVPR*, 2021.
- Jean-Bastien Grill, Florian Strub, Florent Althché, Corentin Tallec, Pierre Richemond, Elena Buchatskaya, Carl Doersch, Bernardo Avila Pires, Zhaohan Guo, Mohammad Gheshlaghi Azar, et al. Bootstrap your own latent—a new approach to self-supervised learning. *Advances in neural information processing systems*, 33:21271–21284, 2020.
- Aditya Grover and Jure Leskovec. node2vec: Scalable feature learning for networks. In *Proceedings of the 22nd ACM SIGKDD international conference on Knowledge discovery and data mining*, pp. 855–864, 2016.
- David Ha, Andrew Dai, and Quoc V. Le. Hypernetworks, 2016.
- Raia Hadsell, Sumit Chopra, and Yann LeCun. Dimensionality reduction by learning an invariant mapping. In *CVPR*, 2006.
- Will Hamilton, Zhitao Ying, and Jure Leskovec. Inductive representation learning on large graphs. *Advances in neural information processing systems*, 30, 2017.
- Kaveh Hassani and Amir Hosein Khasahmadi. Contrastive multi-view representation learning on graphs. In *International conference on machine learning*, pp. 4116–4126. PMLR, 2020.
- Kaiming He, Xiangyu Zhang, Shaoqing Ren, and Jian Sun. Delving deep into rectifiers: Surpassing human-level performance on imagenet classification. In *Proceedings of the IEEE international conference on computer vision*, pp. 1026–1034, 2015.
- Kaiming He, Haoqi Fan, Yuxin Wu, Saining Xie, and Ross Girshick. Momentum contrast for unsupervised visual representation learning. In *CVPR*, 2020.
- Geoffrey Hinton, Oriol Vinyals, and Jeffrey Dean. Distilling the knowledge in a neural network. In *NIPS Deep Learning and Representation Learning Workshop*, 2015.
- R Devon Hjelm, Alex Fedorov, Samuel Lavoie-Marchildon, Karan Grewal, Adam Trischler, and Yoshua Bengio. Learning deep representations by mutual information estimation and maximization. In *ICLR*, 2019.
- Weihua Hu, Bowen Liu, Joseph Gomes, Marinka Zitnik, Percy Liang, Vijay Pande, and Jure Leskovec. Strategies for pre-training graph neural networks. *arXiv preprint arXiv:1905.12265*, 2019.
- Jiabo Huang, Qi Dong and Shaogang Gong, and Xiatian Zhu. Unsupervised deep learning by neighbourhood discovery. In *ICML*, 2019.
- Sergey Ioffe and Christian Szegedy. Batch normalization: Accelerating deep network training by reducing internal covariate shift. In *International conference on machine learning*, pp. 448–456. pmlr, 2015.
- Baoyu Jing, Chanyoung Park, and Hanghang Tong. Hdmi: High-order deep multiplex infomax. In *Proceedings of the Web Conference 2021*, pp. 2414–2424, 2021.
- Diederik P Kingma and Jimmy Ba. Adam: A method for stochastic optimization. *arXiv preprint arXiv:1412.6980*, 2014.

-
- Thomas N Kipf and Max Welling. Semi-supervised classification with graph convolutional networks. *arXiv preprint arXiv:1609.02907*, 2016a.
- Thomas N Kipf and Max Welling. Variational graph auto-encoders. *arXiv preprint arXiv:1611.07308*, 2016b.
- Namkyeong Lee, Junseok Lee, and Chanyoung Park. Augmentation-free self-supervised learning on graphs. In *Proceedings of the AAAI Conference on Artificial Intelligence*, volume 36, pp. 7372–7380, 2022.
- Derek Lim, Joshua Robinson, Lingxiao Zhao, Tess Smidt, Suvrit Sra, Haggai Maron, and Stefanie Jegelka. Sign and basis invariant networks for spectral graph representation learning. *arXiv preprint arXiv:2202.13013*, 2022.
- Shuai Lin, Chen Liu, Pan Zhou, Zi-Yuan Hu, Shuojia Wang, Ruihui Zhao, Yefeng Zheng, Liang Lin, Eric Xing, and Xiaodan Liang. Prototypical graph contrastive learning. *IEEE Transactions on Neural Networks and Learning Systems*, 2022.
- Renming Liu, Semih Cantürk, Olivier Lapointe-Gagné, Vincent Létourneau, Guy Wolf, Dominique Beaini, and Ladislav Rampásek. Graph positional and structural encoder. *arXiv preprint arXiv:2307.07107*, 2023a.
- Yue Liu, Xihong Yang, Sihang Zhou, Xinwang Liu, Siwei Wang, Ke Liang, Wenxuan Tu, and Liang Li. Simple contrastive graph clustering. *IEEE Transactions on Neural Networks and Learning Systems*, 2023b.
- Ilya Loshchilov and Frank Hutter. Decoupled weight decay regularization. *arXiv preprint arXiv:1711.05101*, 2017.
- Ishan Misra and Laurens van der Maaten. Self-supervised learning of pretext-invariant representations. In *CVPR*, 2020.
- Zhen Peng, Wenbing Huang, Minnan Luo, Qinghua Zheng, Yu Rong, Tingyang Xu, and Junzhou Huang. Graph representation learning via graphical mutual information maximization. In *Proceedings of The Web Conference 2020*, pp. 259–270, 2020.
- Bryan Perozzi, Rami Al-Rfou, and Steven Skiena. Deepwalk: Online learning of social representations. In *Proceedings of the 20th ACM SIGKDD international conference on Knowledge discovery and data mining*, pp. 701–710, 2014.
- Ladislav Rampásek, Michael Galkin, Vijay Prakash Dwivedi, Anh Tuan Luu, Guy Wolf, and Dominique Beaini. Recipe for a general, powerful, scalable graph transformer. *Advances in Neural Information Processing Systems*, 35:14501–14515, 2022.
- Fan-Yun Sun, Jordan Hoffmann, Vikas Verma, and Jian Tang. Infograph: Unsupervised and semi-supervised graph-level representation learning via mutual information maximization. *arXiv preprint arXiv:1908.01000*, 2019.
- Mengying Sun, Jing Xing, Huijun Wang, Bin Chen, and Jiayu Zhou. Mocl: Contrastive learning on molecular graphs with multi-level domain knowledge. *arXiv preprint arXiv:2106.04509*, 9, 2021.
- Shantanu Thakoor, Corentin Tallec, Mohammad Gheshlaghi Azar, Mehdi Azabou, Eva L Dyer, Remi Munos, Petar Veličković, and Michal Valko. Large-scale representation learning on graphs via bootstrapping. *arXiv preprint arXiv:2102.06514*, 2021.
- Yonglong Tian, Dilip Krishnan, and Phillip Isola. Contrastive multiview coding. In *Computer Vision—ECCV 2020: 16th European Conference, Glasgow, UK, August 23–28, 2020, Proceedings, Part XI 16*, pp. 776–794. Springer, 2020.
- Aaron van den Oord, Yazhe Li, and Oriol Vinyals. Representation learning with contrastive predictive coding. *arXiv preprint arXiv:1807.03748*, 2018.
- Petar Veličković, Guillem Cucurull, Arantxa Casanova, Adriana Romero, Pietro Lio, and Yoshua Bengio. Graph attention networks. *arXiv preprint arXiv:1710.10903*, 2017.
- Petar Veličković, William Fedus, William L Hamilton, Pietro Liò, Yoshua Bengio, and R Devon Hjelm. Deep graph infomax. *arXiv preprint arXiv:1809.10341*, 2018.

-
- Haonan Wang, Jieyu Zhang, Qi Zhu, Wei Huang, Kenji Kawaguchi, and Xiaokui Xiao. Single-pass contrastive learning can work for both homophilic and heterophilic graph, 2023.
- Zhirong Wu, Yuanjun Xiong, Stella Yu, , and Dahua Lin. Unsupervised feature learning via non-parametric instance discrimination. In *CVPR*, 2018.
- Junyuan Xie, Ross Girshick, and Ali Farhadi. Unsupervised deep embedding for clustering analysis. In *ICML*, 2016.
- Keyulu Xu, Weihua Hu, Jure Leskovec, and Stefanie Jegelka. How powerful are graph neural networks? *arXiv preprint arXiv:1810.00826*, 2018.
- Xueting Yan, Ishan Misra, Abhinav Gupta, Deepti Ghadiyaram, and Dhruv Mahajan. Clusterfit: Improving generalization of visual representations. In *CVPR*, 2020.
- Jianwei Yang, Devi Parikh, and Dhruv Batra. Joint unsupervised learning of deep representations and image clusters. In *CVPR*, 2016.
- Mang Ye, Xu Zhang, Pong C Yuen, and Shih-Fu Chang. Unsupervised embedding learning via invariant and spreading instance feature. In *CVPR*, 2019.
- Yuning You, Tianlong Chen, Yongduo Sui, Ting Chen, Zhangyang Wang, and Yang Shen. Graph contrastive learning with augmentations. *Advances in Neural Information Processing Systems*, 33:5812–5823, 2020.
- Jure Zbontar, Li Jing, Ishan Misra, Yann LeCun, and Stéphane Deny. Barlow twins: Self-supervised learning via redundancy reduction. In *International Conference on Machine Learning*, pp. 12310–12320. PMLR, 2021.
- Sheng Zhou, Hongjia Xu, Zhuonan Zheng, Jiawei Chen, Jiajun Bu, Jia Wu, Xin Wang, Wenwu Zhu, Martin Ester, et al. A comprehensive survey on deep clustering: Taxonomy, challenges, and future directions. *arXiv preprint arXiv:2206.07579*, 2022.
- Jiong Zhu, Yujun Yan, Lingxiao Zhao, Mark Heimann, Leman Akoglu, and Danai Koutra. Beyond homophily in graph neural networks: Current limitations and effective designs. *Advances in neural information processing systems*, 33:7793–7804, 2020a.
- Qi Zhu, Yidan Xu, Haonan Wang, Chao Zhang, Jiawei Han, and Carl Yang. Transfer learning of graph neural networks with ego-graph information maximization. *arXiv preprint arXiv:2009.05204*, 2020b.
- Yanqiao Zhu, Yichen Xu, Feng Yu, Qiang Liu, Shu Wu, and Liang Wang. Deep graph contrastive representation learning. *arXiv preprint arXiv:2006.04131*, 2020c.
- Yanqiao Zhu, Yichen Xu, Qiang Liu, and Shu Wu. An empirical study of graph contrastive learning. *arXiv preprint arXiv:2109.01116*, 2021a.
- Yanqiao Zhu, Yichen Xu, Feng Yu, Qiang Liu, Shu Wu, and Liang Wang. Graph contrastive learning with adaptive augmentation. In *Proceedings of the Web Conference 2021*, pp. 2069–2080, 2021b.
- Chengxu Zhuang, Alex Lin Zhai, and Daniel Yamins. Local aggregation for unsupervised learning of visual embeddings. In *ICCV*, 2019.

A Method

A.1 Preliminary

Nonlinear and Fine-tuning Evaluation Protocols. Nonlinear probing mirrors the linear probing approach but adopts an MLP or a kNN classifier. In fine-tuning, either all or the last few layers of the pre-trained f_θ are updated based on backpropagations computed from the downstream task.

Graph Classification and Link-level Prediction. Graph downstream tasks encompass node classification, graph classification, or link-level prediction. Graph classification typically involves learning node representations followed by a pooling mechanism to compute the graph representation. Link-level prediction can be simplified into node-level tasks aggregating representations from the two end nodes of a specific link. Hence, while ExGRG primarily focuses on node representation learning, its framework can be extended to facilitate the acquisition of graph-level or node-pairwise representations tailored for link-level tasks.

LapPE. This encoding is derived from eigenvectors of the source graph’s Laplacian corresponding to the k -lowest non-zero eigenvalues (Dwivedi et al., 2023).

RWSE. Specifically, the k -th RWSE reflects the probability of returning to the starting state of a random walk after precisely k steps (Dwivedi et al., 2021; Liu et al., 2023a).

SignNet. Utilizing eigenvectors, SignNet is a sign-invariant network proposed to handle varying numbers of sign-ambiguous eigenvectors (Lim et al., 2022; Rampášek et al., 2022).

A.2 Explicit Compositional Relation Graph

Our methodology involves initially generating relation graphs from various sources using different construction algorithms. Subsequently, we aggregate all these relation graphs simply through a learnable linear combination to form a comprehensive relation graph \mathbf{G} , which is then applied in the invariance term. Generally, potential sources for the \mathbf{G} generation process encompass representations \mathbf{Z} , embeddings \mathbf{H} , node features \mathbf{X}^s or \mathbf{X} , intermediate hidden features, and the embeddings of another latent space projection, such as nodes’ PSEs. Some sources, like the adjacency matrix \mathbf{A}^s or data augmentation, require no further processing. However, other sources necessitate processing through a so-called construction algorithm, such as kNN or a clustering-based method.

A.3 Laplacian Eigenmap

$$\mathbf{Z}^* = \underset{\mathbf{Z}}{\operatorname{argmin}} \operatorname{Tr}(\mathbf{Z}^T \mathbf{L} \mathbf{Z}) \text{ s.t. } \mathbf{Z}^T \mathbf{D} \mathbf{Z} = \mathbf{I}, \quad (14)$$

where $\mathbf{D} = \mathbf{V} \mathbf{I} = 2 \mathbf{I}$ and $\mathbf{L} = \mathbf{D} - \mathbf{G}$ are degree and Laplacian matrices for \mathbf{G} , while \mathbf{Z}^* is the optimal LE embeddings.

A.4 Neighborhood Similarity in the Representation Space

Our preliminary experiments indicate that the kNN graph on \mathbf{H} provides more informative relations compared to \mathbf{Z} . We speculate that due to the invariance term, the points in \mathbf{Z} are compelled to be excessively close; therefore, the distance between corresponding points in \mathbf{H} is more instructive for constructing a relation graph.

A.5 Higher-Order Graph Encodings

A.5.1 Adjacency-based Relation Graph

The relation matrix \mathbf{G}^A , based on the adjacency information of the source graph, is defined in 3.3.2. Intuitively, \mathbf{G}^A can provide independent guidance for a standalone relation matrix with increased confidence, especially in datasets exhibiting more homophily. Conversely, using \mathbf{G}^k directly in heterophilic graph datasets might be more beneficial, as all entries in \mathbf{G}^A are likely zero with higher confidence. This is because, in a heterophilic graph, neighboring nodes in the input do not share the same class label, making the overlap between nodes that are neighbors in both the representation kNN graph and the source graph less probable.

A.5.2 PSE-based Relation Graph

The efficacy of various \mathbf{G}^{PSE} depends on the dataset and domain under consideration. Our strategy for employing PSEs diverges from their conventional application in transformers. Nevertheless, a similar impact can be observed when utilizing PSEs in transformers, where the performance of RWSE proves advantageous for small molecular data, while LapPE excels in tasks involving image superpixels and those requiring long-range dependencies. In addition, SignNet with DeepSet encodings demonstrates success across diverse domains and tasks (Rampášek et al., 2022; Liu et al., 2023a).

A.6 Deep Clustering

To obtain the codes \mathbf{Q} , we follow the approach outlined in Asano et al. (2019) and Caron et al. (2020). This is performed by solving the optimization problem by maximizing the similarity between representations and prototypes, with \mathbf{Q}^* representing the optimal solution as

$$\mathbf{Q}^* = \underset{\mathbf{Q}}{\operatorname{argmax}} \operatorname{Tr}(\mathbf{Q}^T \mathbf{C} \mathbf{H}^T) + \epsilon \mathcal{H}(\mathbf{Q}). \quad (15)$$

The term $\mathcal{H}(\mathbf{Q}) = -\sum_{i,j} \mathbf{Q}_{i,j} \log \mathbf{Q}_{i,j}$ represents the entropy of \mathbf{Q} , while ϵ serves as a balancing factor, determining the significance of achieving a uniformly distributed partition through entropy maximization. This involves imposing a constraint on the codes \mathbf{Q} to lie within the transportation polytope, indicating that our codes \mathbf{Q} should adhere to a set \mathcal{Q} , where

$$\mathcal{Q} = \left\{ \mathbf{Q} \in \mathbb{R}_+^{N \times K} \mid \mathbf{Q}^T \mathbf{1}_N = \frac{1}{K} \mathbf{1}_K, \mathbf{Q} \mathbf{1}_K = \frac{1}{N} \mathbf{1}_N \right\}. \quad (16)$$

This constraint implies that, on average, each cluster is expected to be assigned approximately $\frac{N}{K}$ data points, reflecting an equal distribution. To determine a suitable \mathbf{Q} as a solution for Eq. 15 and 16, we leverage the Sinkhorn-Knopp algorithm (Cuturi, 2013). Therefore, we iteratively calculate two renormalization vectors, $\mathbf{u} \in \mathbb{R}^N$ and $\mathbf{v} \in \mathbb{R}^K$, to address the optimization problem as

$$\mathbf{Q}^* = \operatorname{Diag}(\mathbf{u}) \exp\left(\frac{\mathbf{C} \mathbf{H}^T}{\epsilon}\right) \operatorname{Diag}(\mathbf{v}). \quad (17)$$

A.7 End-to-End Training Procedure

A.7.1 SG Mechanism

In the presence of a gradient path through the invariance term \mathcal{L}_I , the optimizer incentivizes the reduction of $\mathbf{G}^{(i)}$ entries. However, it is essential to note that these specific entries within $\mathbf{G}^{(i)}$ are a refined sparse subset derived from a potentially dense $N \times N$ relation matrix. The existence of such a gradient path to update $\mathbf{G}^{(i)}$ generator parameters implies the promotion of weaker relations among instances that initially exhibit strong relations. Inspired by Grill et al. (2020) and Chen & He (2021), to simultaneously optimize both sets of parameters, we propose an SG mechanism specifically on the $\mathbf{G}^{(i)}$ generator parameters (Eq. 9), such as the prototypes \mathbf{C} for \mathbf{G}^O , through the \mathcal{L}_I path. Without this SG, we counter-intuitively diminish the $\mathbf{G}^{(i)}$ entries for candidate pairs with high potential for closer representations.

A.7.2 Relation Matrix Regularization

To ensure the end-to-end aggregation of different relation matrices for deriving the final relation matrix \mathbf{G} , the aggregator module Ψ_ψ gets updates through the invariance term \mathcal{L}_I . The incentive here mirrors the one encountered with each individual relation matrix $\mathbf{G}^{(i)}$ in A.7.1, wherein, lacking constraints, the optimizer tends to converge all \mathbf{G} entries to a trivial solution. To mitigate this, we propose the incorporation of a regularizer aimed at discouraging the entries of \mathbf{G} from collapsing to the degenerate solution, wherein all entries converge to zero. This regularizer is formulated based on the concept of the summation of all \mathbf{G} entries demonstrated in Eq. 12.

Table 3: Statistics of the employed datasets.

Statistic	WikiCS	AmzComp	AmzPhoto	CoCS	CoPhy	Cora	CiteSeer	PubMed	DBLP
# Nodes	11,701	13,752	7,650	18,333	34,493	2,708	3,327	19,717	17,716
# Edges	216,123	574,418	287,326	327,576	991,848	5,429	4,732	44,338	105,734
# Classes	10	10	8	15	5	7	6	3	4
# Features	300	767	745	6,805	8,451	1,433	3,703	500	1,639

A.7.3 Overall Multi-term Loss Objective

During optimization of \mathcal{L}_{ETE} , parameters θ of the encoder f_θ and ϕ of the expander g_ϕ undergo updates through \mathcal{L}_V , \mathcal{L}_C , \mathcal{L}_I , and \mathcal{L}_O . The prototypes \mathbf{C} receive updates through \mathcal{L}_O , while the aggregation module parameters, including ψ for Ψ_ψ , are updated through \mathcal{L}_R and invariance term \mathcal{L}_I .

B Experimental Evaluation

B.1 Datasets

Our node classification experiments encompass evaluations on 9 datasets: WikiCS, Amazon Computers (AmzComp), Amazon Photo (AmzPhoto), Coauthor CS (CoCS), Coauthor Physics (CoPhy), Cora, Citeseer, PubMed, and DBLP. The corresponding statistics for these datasets, such as the number of nodes, edges, classes, and features, are provided in Table 3. Furthermore, if a specific dataset is not used to evaluate a particular method, the corresponding cell is left blank in Table 1.

B.2 SSL Encoder

We employ the GCN proposed in Kipf & Welling (2016a) as the SSL encoder f_θ . Specifically, the output of the l -th GCN layer, $H^{(l)}$, is expressed as

$$H^{(l)} = \text{GCN}^{(l)}(\mathbf{X}, \mathbf{A}) = \sigma(\hat{\mathbf{D}}^{-1/2} \hat{\mathbf{A}} \hat{\mathbf{D}}^{-1/2} \mathbf{X} \mathbf{W}^{(l)}). \quad (18)$$

Here, $\hat{\mathbf{A}} = \mathbf{A} + \mathbf{I}$ represents the adjacency matrix in the presence of self-loops. Additionally, we denote the degree matrix as $\hat{\mathbf{D}} = \sum_i \hat{\mathbf{A}}_i$, nonlinear activation function as σ , and trainable parameters as $\mathbf{W}^{(l)}$, eventually forming parameters θ .

B.3 Downstream Evaluation

To employ an SSL model for a downstream node classification task, the encoder f_θ and expander g_ϕ undergo joint training without utilizing labels \mathbf{Y}^s , effectively following an unsupervised approach for a predetermined number of iterations. Subsequently, the expander g_ϕ is discarded, likely to leverage more generalized representations. The fixed representations obtained from the encoder f_θ , in addition to the labels \mathbf{Y}^s , are employed to train a logistic regression classifier in the graph domain in contrast to the linear layer counterpart used in vision applications (Thakoor et al., 2021). This classifier is trained on top of the frozen representations and, subsequently, evaluated on a validation split to determine optimal hyperparameters. Finally, the node classification accuracy is assessed on a separate test set. This entire process is repeated for 20 trials, each characterized by random model initialization and different train-validation-test splits. The randomness is introduced due to the notable variability observed in computed accuracy across different splits in graphs.

B.4 Additional Evaluation Metrics

In certain instances, the accuracy of the graph datasets exhibits a degree of resilience to alterations in the model. This observation underscores the need to consider our defined metrics for a more comprehensive comparison of different scenarios, including our ablated models. These metrics are computed on both \mathbf{H} and \mathbf{Z} , providing

Table 4: Ablation studies on CiteSeer. Models are altered concerning ExGRG (5k iters) as the reference.

[Ablated] Model	Accuracy	corr \mathbf{H}	corr \mathbf{Z}	std \mathbf{H}	std \mathbf{Z}	nstd \mathbf{H}	rank \mathbf{H}	rank \mathbf{Z}
ExGRG (10k iters)	89.68 \pm 1.46	0.0000	0.0163	0.0547	0.3335	0.0233	956	976
ExGRG (5k iters)	88.61 \pm 1.47	0.0001	0.0138	0.0514	0.2799	0.0211	894	976
Binary \mathbf{G}	84.57 \pm 1.11	0.1491	0.0004	0.1150	0.0509	0.0258	237	627
No \mathcal{L}_R	83.96 \pm 1.51	1.1409	0.0000	0.1847	0.0128	0.0231	103	578
No Ψ_ψ	84.05 \pm 1.43	1.1408	0.0000	0.1847	0.0127	0.0231	103	588
No F_{SG} on \mathbf{G}^S	88.48 \pm 1.42	0.0001	0.0135	0.0512	0.2759	0.0210	890	972
No Standalone \mathbf{G}^k	88.47 \pm 1.42	0.0001	0.0135	0.0512	0.2759	0.0210	890	972
No $\mathbf{G}^{A'}$ or $\mathbf{G}^{R'}$	86.69 \pm 1.12	0.0002	0.0030	0.0526	0.1747	0.0193	791	988
No \mathbf{G}^a	84.35 \pm 1.32	1.2491	0.0000	0.1852	0.0126	0.0232	99	598
No $\mathbf{G}^{A'}$	84.20 \pm 1.27	1.2497	0.0000	0.1853	0.0125	0.0232	99	618
No \mathbf{G}^L	85.67 \pm 1.19	0.0002	0.0054	0.0540	0.1899	0.0208	737	902
No $\mathbf{G}^{R'}$	87.92 \pm 1.51	0.0001	0.0124	0.0560	0.2697	0.0216	864	969
\mathbf{G}^R instead of $\mathbf{G}^{R'}$	83.98 \pm 1.79	0.5892	0.0000	0.1579	0.0146	0.0279	110	1043
No \mathbf{G}^S	88.11 \pm 1.44	0.0001	0.0125	0.0568	0.2702	0.0214	862	971
No \mathbf{G}^{PSE} or $\mathbf{G}^{A'}$	87.90 \pm 1.48	0.0001	0.0124	0.0560	0.2697	0.0215	864	969
No \mathbf{G}^O	88.57 \pm 1.47	0.0001	0.0120	0.0521	0.2671	0.0204	883	974
F_k instead of F_K in \mathbf{G}^O	88.48 \pm 1.42	0.0001	0.0135	0.0512	0.2759	0.0210	890	972
$S_O = \{(i,j) \mid i=j\}$	88.50 \pm 1.42	0.0001	0.0135	0.0512	0.2759	0.0210	890	972
$S_O = S_a$	88.35 \pm 1.25	0.0001	0.0135	0.0512	0.2759	0.0210	890	972
Intra Relations	89.38 \pm 1.25	0.0000	0.0159	0.0542	0.3273	0.0232	955	975

deeper insights into their characteristics. Reported evaluation metrics are inspired by how VICReg criteria in Eq. 1 contribute to constructing the representations.

The **corr** metric measures a notion of correlation among different pairs of features. This is inspired by \mathcal{L}_C , representing the average over squared off-diagonal entries of the covariance matrix corresponding to each pair of feature dimensions. The **std** metric calculates the average standard deviation along each feature dimension. The **nstd** metric captures the same notion of average standard deviation as *std* but on the L_2 -normalized representations. Given the utilization of Euclidean similarity in constructing the embeddings \mathbf{Z} , vector norms also encode information. Therefore, **nstd** is exclusively reported for \mathbf{H} . The **rank** metric corresponds to the rank of the representations, capturing dimensional collapse. Generally, a desirable model exhibits higher values for accuracy’s mean, std, nstd, and rank while demonstrating lower values for corr and accuracy’s standard deviation.

B.5 Ablation Studies

Followings are the direct impact of our ablations on the overall performance, including downstream accuracy and our defined metrics in § B.4. These are reported based on the ablations on Amazon Computers in Table 2 and slightly differ from observations in CiteSeer (Table 4) and Cora (Table 5).

ExGRG (X k iters) signifies the reference model trained with X thousand(s) iterations. To maintain consistency in comparison, all ablated models listed in other rows should be assessed relative to *ExGRG (5k iters)*, ensuring an equal number of iterations for reference. The **Binary \mathbf{G}** model enforces strict binary values (0 or 1) for all entries in \mathbf{G} , unlike the soft version of ExGRG. This results in a slight decrease in accuracy, coupled with a notable increase in corr \mathbf{H} , significantly lower std \mathbf{Z} , lower ranks, and slightly decreased nstd. **No \mathcal{L}_R** eliminates the \mathbf{G} regularization loss, leading to reduced accuracy, notably increased corr \mathbf{H} , a substantial decrease in std \mathbf{Z} , a slight dip in nstd, and significantly lower ranks, indicating a dimensional collapse. **No Ψ_ψ** removes the online aggregator Ψ_ψ , implying that parameters λ_i become hyperparameters, fixed throughout training. This results in diminished accuracy, elevated corr \mathbf{H} , collapse indicated by low ranks, and reduced std \mathbf{Z} and nstd. **No F_{SG}**

Table 5: Ablation studies on Cora. Models are altered concerning ExGRG (5k iters) as the reference.

[Ablated] Model	Accuracy	corr H	corr Z	std H	std Z	nstd H	rank H	rank Z
ExGRG (5k iters)	97.87 \pm 0.55	0.0000	0.0935	0.0281	0.6168	0.0320	946	824
Binary G	93.84 \pm 0.99	5.4081	0.0068	0.2642	0.0661	0.0121	47	43
No \mathcal{L}_R	93.57 \pm 1.09	73.106	0.0065	0.4721	0.0604	0.0272	9	20
No Ψ_ψ	93.61 \pm 1.15	70.161	0.0067	0.4635	0.0607	0.0275	9	21
No F_{SG} on G^S	93.60 \pm 1.25	0.0391	0.0061	0.0897	0.0662	0.0211	217	341
Add Standalone G^k	93.17 \pm 1.16	11.229	0.0131	0.2841	0.1083	0.0171	23	61
No $G^{A'}$ or $G^{R'}$	93.15 \pm 1.19	127.182	0.0072	0.5422	0.0609	0.0229	8	21
No G^a	93.01 \pm 1.17	14.856	0.0081	0.3121	0.0639	0.0258	13	19
No $G^{A'}$	93.18 \pm 1.26	11.759	0.0086	0.2942	0.0649	0.0260	15	20
No G^L	95.65 \pm 1.13	0.2911	0.1888	0.1281	0.2483	0.0118	230	435
No $G^{R'}$	96.16 \pm 1.03	0.0059	0.0646	0.0633	0.3737	0.0178	571	784
G^R instead of $G^{R'}$	93.20 \pm 1.35	0.0386	0.0069	0.0914	0.0679	0.0248	215	305
No G^S	92.79 \pm 1.13	0.0462	0.0086	0.0933	0.0728	0.0249	154	117
No G^{PSE} or $G^{A'}$	95.91 \pm 0.97	0.0067	0.0398	0.0662	0.2916	0.0172	570	783
No G^O	93.10 \pm 0.81	0.3040	0.0082	0.1174	0.0666	0.0259	91	108
F_k instead of F_K in G^O	93.43 \pm 1.06	0.0356	0.0203	0.1039	0.1618	0.0147	272	439
$S_O = \{(i,j) \mid i=j\}$	93.20 \pm 1.24	0.0660	0.0062	0.0919	0.0639	0.0259	176	280
$S_O = S_a$	96.17 \pm 0.91	0.1995	0.0217	0.1089	0.1142	0.0117	256	462
Intra Relations	95.24 \pm 1.07	0.0364	0.0219	0.0712	0.1030	0.0155	220	236

on G^S signifies the absence of the SG mechanism on SignNet, allowing it to be altered from its pre-trained status. This leads to a marginal decrease in accuracy, while the other metric values remain largely unchanged.

Add/No Standalone G^k signifies the addition or removal of a standalone relation matrix G^k solely based on kNN in H . The inclusion of G^k depends on the extent to which the unfiltered kNN graph proves beneficial for a particular dataset. For AmzComp, incorporating G^k leads to reduced accuracy and a slight decrease in std Z . **No $G^{A'}$ or $G^{R'}$** removes any relation graph derived from G^k , encompassing the exclusion of G^A or, in some datasets, the absence of G^R , with details in *Appendix* Table 6 and § B.7. This leads to a minor decrease in accuracy and a slight reduction in std Z . **No G^a** eliminates the relation graph directly based on pairwise augmentation. In this scenario, where the enforcement of identical representations for pairs in S_a is not explicitly present, random augmentations are still applied to two views. Thus, other components, such as G^k may indirectly enforce similarity for pairs in S_a . This leads to a slight decrease in accuracy and a minor reduction in std Z .

No $G^{A'}$ excludes the utilization of adjacency information for constructing a relation matrix. This leads to a slight decrease in accuracy and std Z . **No G^L** eliminates the relation graph based on Laplacian encoding, leading to a marginal decrease in accuracy and std Z . **No $G^{R'}$** eliminates the relation graph based on random walk encoding, resulting in significantly higher corr H , reduced accuracy, std Z , nstd H , and a collapse in ranks. **G^R instead of $G^{R'}$** utilizes the unfiltered version of G^R as opposed to filtering it by computing $G^R \odot G^k$ with details in *Appendix* Table 6 and § B.7. This leads to decreased accuracy and reduced std Z . **No G^S** eliminates the relation graph based on SignNet encoding, leading to a slight decrease in accuracy and a minor reduction in std Z . **No G^{PSE} or $G^{A'}$** omits any utilization of positional or structural properties of the graph, involving neither PSE nor adjacency. This leads to a minor decrease in accuracy and a slight reduction in std Z .

No G^O entirely removes the end-to-end clustering module. This leads to decreased accuracy, notably increased corr H , and significantly reduced std Z . **F_k instead of F_K in G^O** employs an alternative method to sparsify G^O by utilizing the local version F_k instead of the global F_K in Eq. 8. In our proposed setting, the top-K globally highest entries in the entire relation graph are selected, and the rest are set to zero. Here, a kNN-like operation is performed, where, for each data point as an anchor, the top-K largest entries are selected, and the rest are set to zero. This leads to a slight decrease in accuracy and std Z . $S_O = \{(i,j) \mid i=j\}$ and $S_O = S_a$ yield similar outcomes, respectively eliminating augmentation pairs S_a and self pairs ($i=j$) from S_O . The set S_O denotes

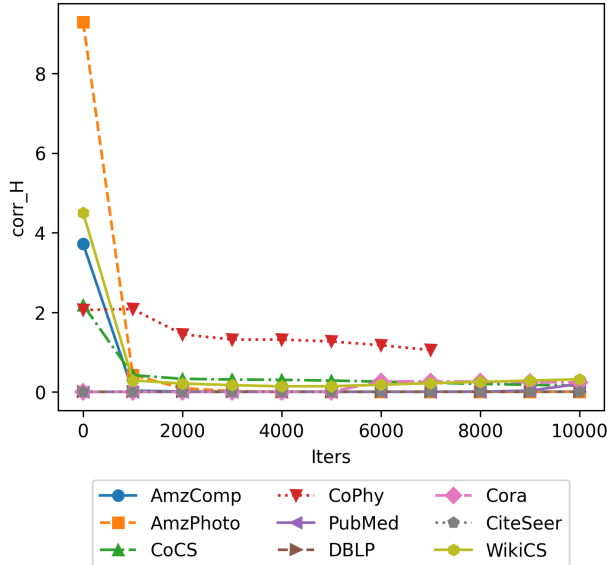


Figure 4: $\text{corr } \mathbf{H}$ vs. iterations throughout the SSL pre-training.

the pairs for applying distribution alignment in the optimal transport loss function. This includes both *self* data points, i.e., $i=j$, and *augmentation* pairs (i,j) . These ablations each eliminate one of these components in the model. This leads to a slight decrease in accuracy and $\text{std } \mathbf{Z}$.

Intra Relations represents a model where all relation graphs $\mathbf{G}^{(i)} \in S_G$ are forced to consider both inter- and intra-view relations. With a fixed GPU memory allocation, the impact of this proposed approach becomes more pronounced in smaller datasets such as CiteSeer and Cora in *Appendix* Tables 4 and 5. The introduction of intra-view relations has the potential to result in the construction of better representations, manifesting in higher accuracy and increased $\text{std } \mathbf{Z}$. In Table 1, the decision on whether to consider intra-relations for each $\mathbf{G}^{(i)}$ is determined independently through balancing with mini-batch size considerations.

B.6 Pre-Training Analysis

This section serves as an extension to § 4.4, delving into the trends observed in correlations, standard deviations, and ranks for representations \mathbf{H} and embeddings \mathbf{Z} .

Correlation. Fig. 4 and 5 illustrate our defined corr metric, resembling the correlation among various pairs of feature dimensions for \mathbf{H} and \mathbf{Z} . Although \mathcal{L}_C targets reducing correlation for \mathbf{Z} , we observe that the correlation among feature dimensions of \mathbf{H} also decreases over iterations. The metric $\text{corr } \mathbf{Z}$ initially experiences a significant decrease and then slightly increases throughout the training. We speculate this behavior is because the correlation is slightly sacrificed after a few thousand iterations to address other aspects of a proper representation.

Standard Deviation. In Fig. 6 and 7, our $nstd$ and std metrics for \mathbf{H} and \mathbf{Z} are presented. A higher standard deviation for representations indicates a wider spread of data points in each feature dimension, reflecting a notion of points’ separability along a particular dimension. The notable drop in $\text{std } \mathbf{Z}$ for Cora aligns with the decrease in accuracy, suggesting that this metric could be an indicator to terminate SSL pre-training. Our ultimate target for $\text{std } \mathbf{Z}$ is 1, corresponding to \mathcal{L}_V . Fig. 7 demonstrates that certain datasets achieve this target within 10k iterations while others progressively move toward this objective throughout the pre-training. Additionally, despite \mathcal{L}_V loss being applied to \mathbf{Z} , Fig. 6 reveals a more or less increasing trend for $nstd \mathbf{H}$.

Rank. Fig. 8 and 9 demonstrates a notion of rank for \mathbf{H} and \mathbf{Z} . This is essentially the normalized version of the introduced $rank$ discussed in § B.4, obtained by dividing the rank by the corresponding D_H or D_Z . Higher ranks signify a more effective utilization of the capacity of the feature dimensions to map the points. With the exception of PubMed, Fig. 9 demonstrates a consistent increase in $nrank$, showcasing the effectiveness of \mathcal{L}_{ETE} . We speculate that the PubMed trend suggests that necessary information could be encoded into lower dimensions,

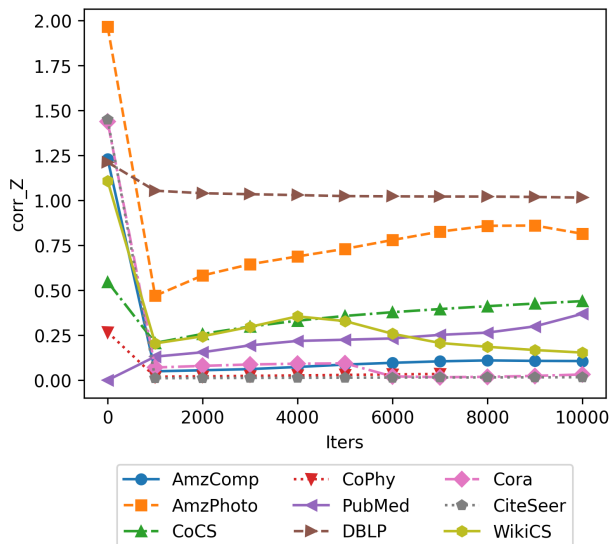


Figure 5: $corr\ Z$ vs. iterations throughout the SSL pre-training.

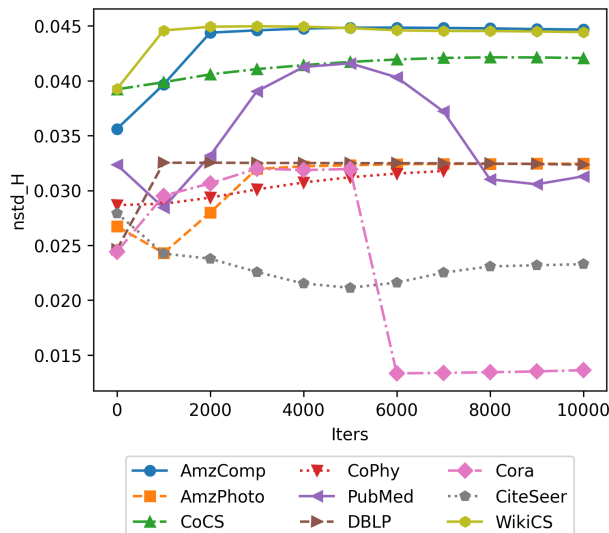


Figure 6: $nstd\ H$ vs. iterations throughout the SSL pre-training.

a phenomenon also reflected in nrank H from Fig. 8. For PubMed, nrank Z increases after an initial drop, closely mirroring the trend observed in accuracy. The corresponding drops in Cora are also likely attributable to over-training, as evidenced by the corresponding accuracy trend on this dataset.

B.7 Selected Hyperparameters

Hyperparameter tuning is conducted to identify optimal parameters for each utilized dataset. The chosen hyperparameters are outlined in Table 6, corresponding to the models whose performance is detailed in Table 1. Due to constraints on the GPU with a 12 GB memory, a limited number of nodes is randomly selected at each iteration to construct the relation graph G ; this quantity is denoted as the mini-batch size N ($G\ B.S.$). The optimizer algorithm utilized for end-to-end model training, including AdamW (Loshchilov & Hutter, 2017) or Adam (Kingma & Ba, 2014) algorithms, is denoted as $Optim$. The learning rate is represented by $L.R.$, and $\#Iters$ signifies the number of iterations used for training the SSL encoder and expander without utilizing labels. No learning scheduler is employed. In the downstream evaluation, mirroring methods like BGRL (Thakoor et al., 2021), the expander is replaced with an L_2 -regularized logistic regression classifier, while the encoder weights remain fixed.

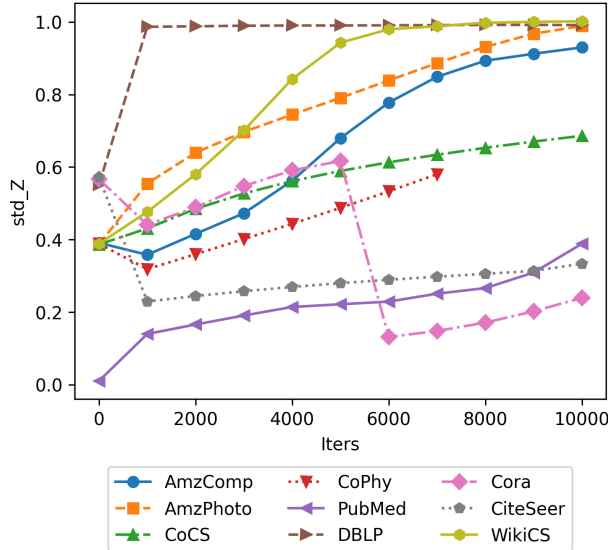


Figure 7: $std\ Z$ vs. iterations throughout the SSL pre-training.

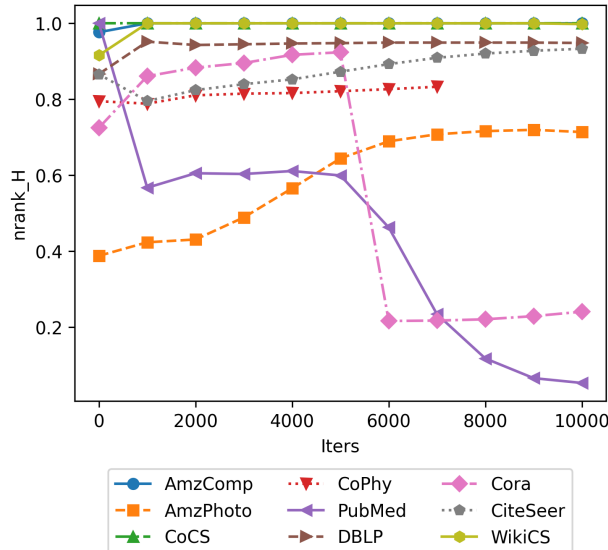


Figure 8: $nrnk\ H$ vs. iterations throughout the SSL pre-training.

The coefficients for the variance, covariance, and invariance loss terms introduced in Eq. 1 and 2 are denoted by α , β , and γ , respectively. We employed various activation functions in the SSL encoder and expander, including PReLU (He et al., 2015), ReLU, and ELU (Clevert et al., 2015). Additionally, for normalization techniques, we utilized BN (Batch Normalization) (Ioffe & Szegedy, 2015) or None (no normalization). The parameters $[f_\theta]$ *Act.*, *Norm.*, *#Lay.*, *#Hid.*, and D_H denote the SSL encoder’s activation function, normalization technique, number of GCN layers, number of features in hidden layers, and representation dimension, i.e., the last GCN output dimension, respectively. The same set of hyperparameters is reported for the expander g_ϕ modeled with an MLP.

The parameter α_2 serves as the coefficient for the relation graph regularization loss term \mathcal{L}_R . Parameters $[\Psi_\psi]$ *#Lay.* and *#Hid./#In* represent the number of layers and the proportion of the hidden to the input dimension of the relation graph aggregator Ψ_ψ .

The augmentation hyperparameters, starting with G^a , are directly inherited from BGRL (Thakoor et al., 2021). The parameters p_i^e and p_i^n represent the probabilities associated with masking edges and node features in the i -th SSL view.

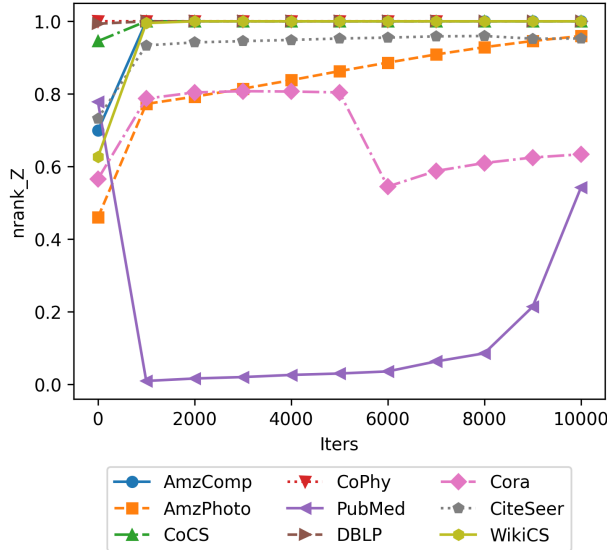


Figure 9: $nrank\ Z$ vs. iterations throughout the SSL pre-training.

Standalone \mathbf{G}^k signifies whether a relation graph exclusively derived from a kNN on representations, denoted as \mathbf{G}^k , is directly utilized. Depending on the noise level in this guidance, its inclusion may enhance performance in certain datasets. For datasets where this parameter is set as *False*, \mathbf{G}^k is still integrated into \mathbf{G}^A to form $\mathbf{G}^{A'}$ and could potentially be incorporated into \mathbf{G}^R based on another boolean parameter denoted as $\mathbf{G}^{R'}$ instead of \mathbf{G}^R . The parameter $[\mathbf{G}^k]$ k represents the value of k used for executing kNN to derive \mathbf{G}^k . Similar notations apply to the determination of k for performing kNNs to obtain \mathbf{G}^L , \mathbf{G}^R , and \mathbf{G}^S .

The parameters $[\mathbf{G}^L]$ *Freq.* and $[\mathbf{G}^S]$ *Freq.* denote the maximum frequency utilized in generating the relation graphs for LapPE and SignNet. The parameter $[\mathbf{G}^S]$ *Arch.* specifies the architecture employed to compute the SignNet PSEs, while $[\mathbf{G}^R]$ *Kernel* represents the specific kernel parameter used in computing RWSEs.

The hyperparameters $[\mathbf{G}^O]$ K , τ , and ϵ correspond to the number of prototypes, softmax temperature in Eq. 5, and the entropy balancing factor in Eq. 15. Additionally, $[\mathbf{G}^O]$ K_g/N denotes the proportion of K_g to the \mathbf{G} mini-batch size used in sparsifying the relation graph \mathbf{G}^O within F_K . For instance, in the case of the Amazon Computers dataset, this parameter is set to 8, and the mini-batch size is 3072, resulting in $K_g = 8 \times 3,072 = 24,578$. The parameter $[\mathbf{G}^O]$ *S.K. #Iters.* represents the number of iterations for the Sinkhorn-Knopp algorithm, and α_1 serves as the coefficient for the optimal transport alignment term \mathcal{L}_O .

B.8 Hyperparameter Analysis

This section extends § 4.4 by delving into an analysis of selected hyperparameters, shedding light on their significance and some valuable insights gained from their impact on downstream performance and other metrics. Since node classification accuracy may not be a sufficiently sensitive metric and is confined to a specific task, we present values for our other predefined metrics outlined in § B.4. These evaluations are conducted explicitly on the Amazon Computers dataset while keeping all other hyperparameters fixed as per Table 6.

Fig. 10 represents a special scenario where $D_H = D_Z$. As we simultaneously alter the feature dimensions of representations and embeddings, we observe a corresponding adjustment in accuracy and the rank of these elements. This underscores the model’s effectiveness in harnessing larger feature dimensions.

In Fig. 11, we explore the impact of the mini-batch size N employed in constructing relation graphs. The consistent stability in accuracy underscores our model’s ability to capture meaningful directions for guiding the invariance term, even with a reduced number of points at each iteration. However, there is a slight improvement in $corr\ \mathbf{H}$, $corr\ \mathbf{Z}$, and $nstd\ \mathbf{H}$ with larger mini-batch sizes. The observed degradation in $std\ \mathbf{Z}$ with larger mini-batch size may be attributed to utilizing the same number of iterations for all models, and this effect could potentially be mitigated with prolonged training, as the variance term \mathcal{L}_V directly compares the spread with 1.

Table 6: Selected hyperparameters utilized for each dataset.

HP	WikiCS	AmzComp	AmzPhoto	CoCS	CoPhy	Cora	CiteSeer	PubMed	DBLP
N (G B.S.)	3072	3072	3072	2560	2048	3072	2048	2560	3072
Optim.	AdamW	AdamW	AdamW	AdamW	AdamW	Adam	Adam	Adam	Adam
L.R.	1e-4	1e-4	5e-5	5e-6	1e-5	5e-4	5e-5	1e-4	5e-4
#Iters.	1000	9000	9000	2000	6000	5000	10000	10000	10000
α [\mathcal{L}_V]	40	100	80	60	60	100	40	80	100
β [\mathcal{L}_C]	10	80	10	10	100	80	100	10	10
γ [\mathcal{L}_I]	5	5	5	5	5	5	5	5	5
$[f_\theta]$ Act.	PReLU	PReLU	PReLU	PReLU	PReLU	ReLU	PReLU	ReLU	ReLU
$[f_\theta]$ Norm.	BN	BN	BN	BN	BN	BN	None	BN	None
$[f_\theta]$ #Lay.	2	2	2	2	2	2	2	2	2
$[f_\theta]$ #Hid.	1024	1024	1024	1024	1024	1024	1024	1024	1024
D_H	512	512	1024	512	512	1024	1024	512	1024
$[g_\phi]$ Act.	PReLU	PReLU	PReLU	PReLU	PReLU	ELU	ELU	ELU	ELU
$[g_\phi]$ Norm.	BN	BN	BN	BN	None	BN	BN	None	BN
$[g_\phi]$ #Lay.	2	2	2	2	2	2	2	2	2
$[g_\phi]$ #Hid.	2048	2048	1024	2048	512	1024	2048	512	512
D_Z	1024	1024	1024	1024	128	1024	2048	1024	1024
α_2 [\mathcal{L}_R]	0.05	0.02	0.5	0.2	2	0.5	0.02	0.2	2
$[\Psi_\psi]$ #Lay.	3	3	3	3	3	4	2	3	4
$[\Psi_\psi]$ #Hid./#In	2	2	2	2	2	2	2	2	2
$[G^a]$ p_1^e	0.2	0.5	0.4	0.3	0.4	0.2	0.2	0.4	0.1
$[G^a]$ p_1^r	0.2	0.2	0.1	0.3	0.1	0.3	0.3	0	0.1
$[G^a]$ p_2^e	0.3	0.4	0.1	0.2	0.1	0.4	0	0.1	0.4
$[G^a]$ p_2^r	0.1	0.1	0.2	0.4	0.4	0.4	0.2	0.2	0
Standalone G^k	False	False	False	False	True	False	True	False	False
$[G^k]$ k	10	12	80	8	64	32	8	4	32
$[G^L]$ k	32	16	8	48	4	8	24	8	48
$[G^L]$ Freq.	40	56	8	32	16	32	64	48	40
$[G^R]$ k	40	64	16	8	32	80	40	56	56
$[G^R]$ Kernel	20	16	8	16	8	24	16	12	20
G^R instead of G^R	True	True	True	True	False	False	True	True	True
$[G^S]$ k	48	32	80	4	8	4	8	32	16
$[G^S]$ Freq.	8	16	24	10	20	10	8	12	10
$[G^S]$ Arch.	DeepSet	DeepSet	MLP	MLP	MLP	DeepSet	MLP	MLP	MLP
$[G^O]$ K	64	64	64	64	64	64	128	64	64
$[G^O]$ τ	0.1	0.1	0.1	0.1	0.1	0.1	0.1	0.1	0.1
$[G^O]$ S.K. #Iters.	6	6	6	6	6	6	6	6	6
$[G^O]$ ϵ	0.05	0.05	0.05	0.05	0.05	0.05	0.05	0.05	0.05
$[G^O]$ K_g/N	32	8	4	14	48	12	32	8	32
$\alpha_1[\mathcal{L}_O]$	1	0.01	0.2	0.01	2	0.2	0.01	0.02	0.5

In Fig. 12, we investigate the impact of varying the parameter k for kNN while utilizing a standalone G^k . This illustration reveals that performance tends to drop as the number of points selected in kNN to guide the invariance loss \mathcal{L}_I becomes excessively large. This decline is attributed to the heightened noise introduced by abundant guidance points in the kNN process.

In Fig. 13, we explore the influence of altering the number of prototypes K in the clustering module. The overall trend highlights the relative stability of downstream accuracy in relation to the choice of the number of clusters, a typically challenging task across different datasets. Moreover, the slightly increasing trend underscores the model’s capability to leverage a higher number of prototypes. Therefore, there is no necessity for tedious tuning specific to each dataset; having a sufficiently large number of prototypes proves to be effective across diverse scenarios.

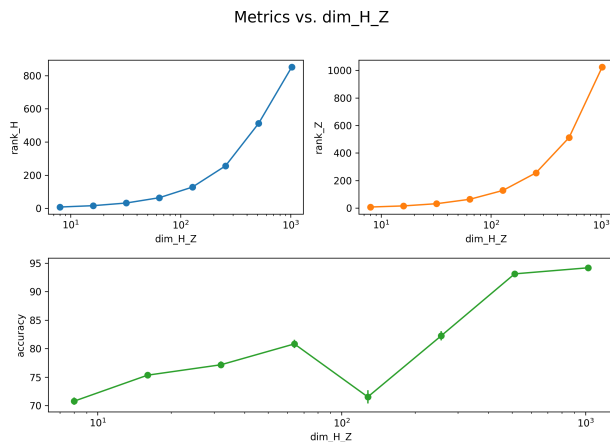


Figure 10: Impact of simultaneously altering D_H and D_Z in the particular case where $D_H = D_Z$ on our metrics and downstream accuracy for Amazon Computers.

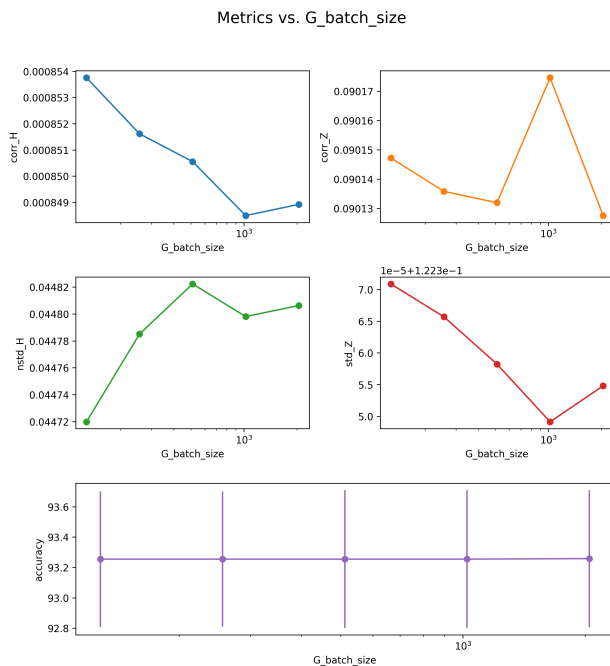


Figure 11: Impact of altering N , G mini-batch size, on our metrics and downstream accuracy for Amazon Computers.

In Fig. 14, we explore the influence of varying α_1 , the coefficient for \mathcal{L}_O . As indicated by this figure and the ablation studies in Table 2, the model exhibits improved performance as long as this loss term is present, with a slightly more recognizable impact within a specific range of the coefficient α_1 . However, over-enforcement of this alignment leads to a worsening performance.

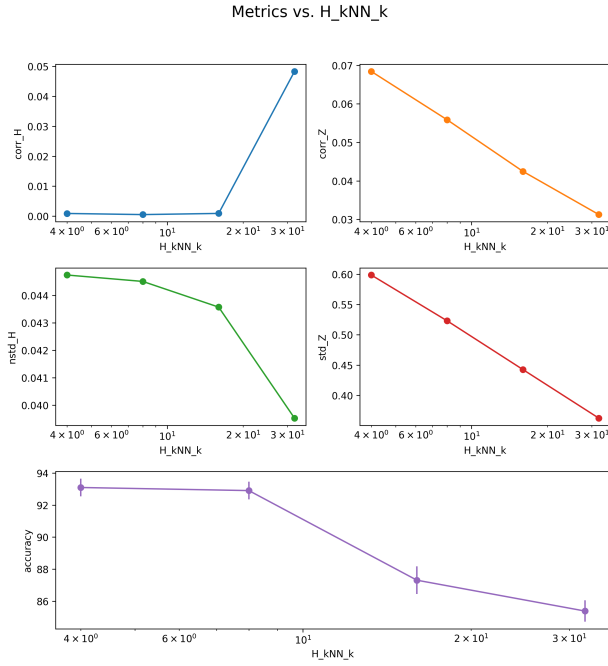


Figure 12: Impact of altering $[G^k]$ k on our metrics and downstream accuracy for Amazon Computers.

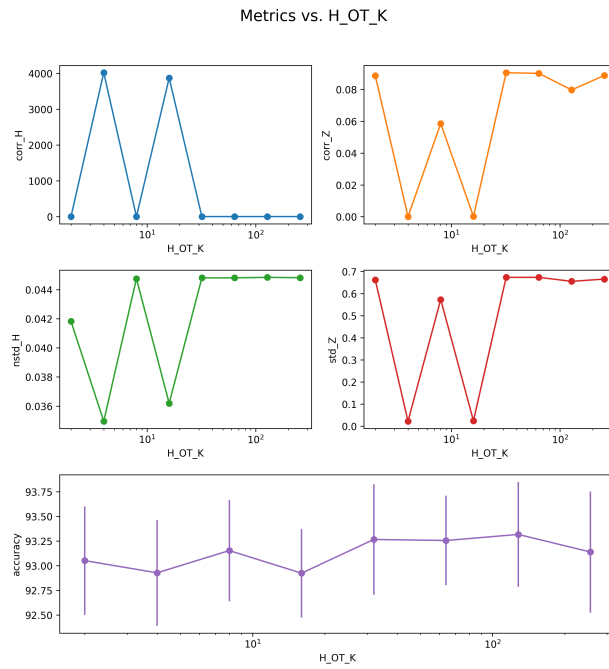


Figure 13: Impact of altering $[G^O]$ K indicating the number of prototypes on our metrics and downstream accuracy for Amazon Computers.

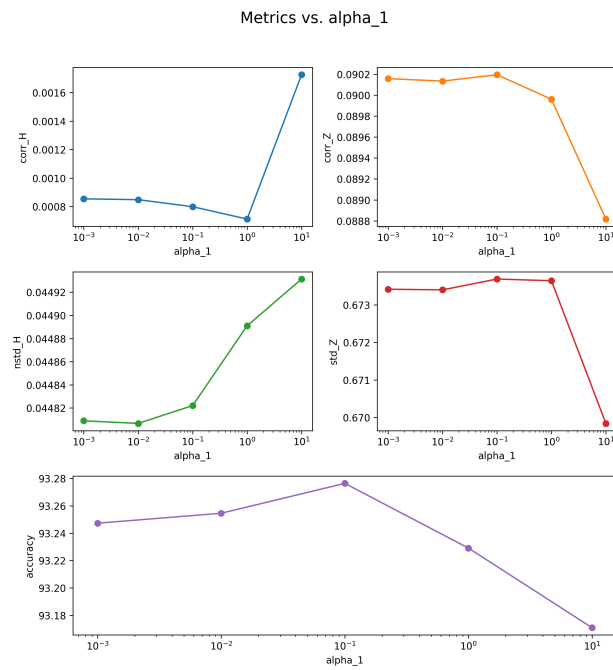


Figure 14: Impact of altering $\alpha_1[\mathcal{L}_O]$ indicating the coefficient for optimal transport alignment term on our metrics and downstream accuracy for Amazon Computers.